The role of midlatitude cyclones in the emission, transport, production, and removal of aerosols in the Northern Hemisphere

Joseph Robinson

A thesis

Submitted in partial fulfillment of the

requirements for the degree of

Master of Science

University of Washington

2022

Committee:

Lyatt Jaeglé

Becky Alexander

Robert Wood

Program authorized to offer degree:

Atmospheric Sciences

University of Washington

Abstract

The role of midlatitude cyclones in the emission, transport, production, and removal of aerosols in the Northern Hemisphere

Joseph Robinson

Chair of the Supervisory Committee:

Lyatt Jaeglé

Department of Atmospheric Sciences

We examine the distribution of aerosol optical depth (AOD) across 27,707 northern hemisphere (NH) midlatitude cyclones for 2005-2018 using retrievals from the Moderate Resolution Spectroradiometer (MODIS) sensors and simulations from the Modern Era Retrospective analysis for Research and Applications, version 2 Global Modeling Initiative (M2GMI) chemical transport model. MODIS AOD and fine mode AOD (fAOD) cyclone-centered composites feature enhancements of 30-50% to the east of the cyclone center in the warm conveyor belt (WCB) airstream. Coarse mode AOD (cAOD) is more than doubled near the center of the cyclone, co-located with high surface wind speeds. Within the WCB, MODIS AOD (fAOD) maximizes at 0.2 (0.09) in spring and summer. M2GMI reproduces this magnitude and seasonality to within 16%. Annually, both MODIS and M2GMI show that fAOD accounts for 68% of AOD enhancement in WCBs while cAOD contributes the other 32%. AOD and fAOD are 60% larger in North Pacific WCBs and show a strong relationship with anthropogenic

pollution. Composite profiles of M2GMI extinction show that sulfate, organic carbon, and dust enhancements maximize in the free troposphere while sea salt maximizes at the surface. Midlatitude cyclones account for 355 Tg yr^{-1} of sea salt aerosol emissions annually, or 60% of the 30-80^{o}N total. We find that largescale precipitation in cyclone WCBs efficiently removes > 90% of sulfate but only 30-40 % of organic carbon and dust. Export of sulfate therefore occurs due to chemical production in the WCB while organic carbon and dust export occurs as a result of transport.

1. Introduction

Tropospheric aerosols exert considerable influence on earth's climate, ecosystems, and human health. Aerosols substantially perturb Earth's radiation balance both directly by scattering and absorbing solar radiation and indirectly by altering cloud properties (Myhre et al., 2013; Partanen, Landry, & Matthews, 2018; Shindell et al., 2013; Smith & Bond, 2014; Westervelt et al., 2015). Nutrients in the form of iron and nitrate aerosols are transported from land and deposited into ocean environments where they can promote primary production (Baker et al., 2003; Jickells & Spokes, 2001). Exposure to increased levels of fine particulate matter has also been shown to result in as many as 4.2 million premature deaths each year globally (Fang et al., 2013; Silva et al., 2017).

Explaining the full spectrum of direct aerosol emissions, secondary formation processes, transport, and removal pathways has therefore been the subject of continual research in recent decades (Alfaro & Gomes, 2001; Andreae & Crutzen, 1997; Graedel & Weschler, 1981; Jacobson & Hansson, 2000; Kerminen et al., 2005; Prather, Hatch, & Grassian, 2008). Despite these efforts, large uncertainties remain in our understanding of these aerosol processes and their representation in models (Guibert et al., 2005; Hodzic et al., 2016; Kinne et al., 2003; Real et al., 2010; Q. Yang et al., 2015). These uncertainties and the resulting differences between modeled and observed aerosol concentrations can become exacerbated by errors in model processes during long-range transport (Brock et al., 2004; Dunlea et al., 2009; Heald et al., 2006; Nam et al., 2010; Peltier et al., 2008).

Midlatitude cyclones are at the intersection of processes controlling the regional and global distribution of tropospheric aerosols. The ability of their warm conveyor belts (WCBs) to lift air masses into the free troposphere and redistribute them globally is a dominant pathway for the export of pollution from Asia and North America (Hannan et al., 2003; Jaffe et al., 2003; Liang et al., 2004; Sinclair, Gray, & Belcher, 2008). Research in recent decades has tried to better characterize the timing and extent of this export as well as its impact on downwind regions (e.g., Ding et al., 2009; Eguchi et al., 2009; Luan & Jaeglé, 2013; Y. Yang, Liao, & Lou, 2015; Yu et al., 2008). For example, Yu et al. (2008) used monthly satellite observations of AOD during a 4-year period to estimate 18 Tg of pollution aerosol is exported from the Asian continent each

year. Luan and Jaeglé (2013) used daily satellite observations and a chemical transport model to examine aerosol transport off both Asia and North America, finding AOD to be enhanced by more than 50% during export events. Precipitation associated with midlatitude cyclones can act to remove soluble aerosols and their precursors (Park et al., 2005). Extensive cloud cover also provides a favorable environment for aerosol formation via aqueous sulfur dioxide (SO_2) oxidation and growth during subsequent transport (Brock et al., 2004; Dunlea et al., 2009). Lastly, strong surface winds within the cyclone can result in enhanced sea spray emissions over oceans (Lewis & Schwartz, 2004).

There has also been recent interest in quantifying the extent to which aerosols themselves influence midlatitude cyclones through their effects on clouds and precipitation. A number of studies have demonstrated the cloud and precipitation structure of cyclones as well as its relationship with aerosols (e.g., Grandey et al., 2011; McCoy et al., 2018; Naud, Posselt, & van den Heever, 2017). For example, McCoy et al. (2018) showed that aerosol-cloud interactions result in an increase in cloud liquid water content, overall cloud coverage, and albedo in midlatitude cyclones in both hemispheres. In addition, a strengthening of midlatitude cyclones in the North Pacific due to the increased abundance of aerosols over the pre-industrial period has either been predicted by modeling studies (Joos et al., 2017; Wang, Zhang, & Saravanan, 2014) or observed as increases in precipitation and the frequency of high clouds (Zhang et al., 2007). For example, Wang, Zhang, & Saravanan (2014) used a multi-scale modeling approach to find precipitation is enhanced by 7-20% in North Pacific winter-time cyclones that occur under a predominantly polluted versus marine aerosol scenario.

Transport mediated by midlatitude cyclones occurs primarily along two coherent airstreams: the WCB and dry intrusion (DI). The WCB is the major ascending airstream of midlatitude cyclones (Browning & Roberts, 1994); it originates in the warm sector of the cyclone out ahead of the cold front and rapidly ascends moist isentropically from the boundary layer to the middle and upper troposphere as it travels poleward (Eckhardt et al., 2004; Stohl, 2001). Lifting of warm, moist air in the WCB results in widespread cloud cover and intense precipitation that culminates in a hallmark comma-shaped structure (Catto, Shaffrey, & Hodges, 2010; Whitaker, Uccellini, & Brill, 1988). In the upper troposphere, the WCB can turn anticyclonically in the stronger

westerly flow or turn cyclonically and become aligned vertically with the surface low (Whitaker et al., 1988). Conversely, the DI originates in the upper troposphere or lower stratosphere and descends while fanning out behind the surface cold front. Downward transport of cold, dry air leads to little cloud cover and the presence of the "dry slot" as viewed on true color satellite imagery (Browning, 1997).

In the present study, our aim is to systematically examine the processes affecting aerosol optical depth (AOD) distributions within NH midlatitude cyclones. The primary tool we use to accomplish this aim is cyclone-centered compositing across 27,707 midlatitude cyclones over a 14-year period (2005-2018). We composite these individual cyclone cases to analyze AOD as observed by the Moderate Resolution Imaging Spectroradiometer (MODIS) sensors aboard the NASA Terra and Aqua satellites. We compare the resulting AOD composites to simulations from the NASA Modern Era Retrospective analysis for Research and Applications, version 2 Global Modeling Initiative (M2GMI) global chemical transport model and use these simulations to interpret the observed structures in the AOD composites.

Grandey et al. (2011) built midlatitude cyclone composites of satellite AOD and showed a strong positive relationship between AOD and surface wind speeds within the cyclone, confirming midlatitude cyclones are indeed a major emission pathway for sea salt particles. In a separate analysis, Grandey et al. (2013) found a positive relationship between cloud coverage and AOD in North Atlantic cyclones, but a negative relationship between AOD and cloud top temperature. They concluded that storm structure and strength could only explain a small fraction of these relationships and that aerosol-cloud interactions were likely part of the cause. More recently, Naud, Posselt, & van den Heever (2016) examined the distribution of MODIS AOD using composites of midlatitude cyclones over the NH oceans, focusing on the interactions between AOD, clouds, and precipitation. They found a positive relationship between AOD and cloud cover in NH midlatitude cyclones and noted that largest AOD values often occur along frontal boundaries within the cyclone domain where precipitating clouds form. We build upon these previous studies by quantifying the extent to which the midlatitude cyclone environment induces primary aerosol emissions, processes aerosols, and ultimately results in aerosol export to the global atmosphere.

In section 2 we describe the MODIS observations and model datasets used in our analysis. We present our cyclone identification methodology and sampling and compositing approach in section 3. In section 4 we analyze AOD composites obtained from MODIS observations and M2GMI simulations and examine the seasonal variation of AOD within cyclone WCBs. In section 5 we use vertical profiles of aerosol extinction from M2GMI to examine how enhancements vary throughout the troposphere. In section 6 we use M2GMI to quantify the contributions of midlatitude cyclones to sea salt aerosol emissions and AOD enhancements before summarizing in section 7.

2. Observations and Models

2.1 MODIS AOD Observations

We use AOD retrievals from the MODIS instruments onboard the NASA Terra and Aqua satellites (Remer et al., 2005). Both platforms orbit at an altitude of 705 km with a 16 day repeat cycle. Terra has an equatorial crossing time in the morning (10:30 local) while the Aqua equatorial crossing is in the afternoon (13:30 local). MODIS measures reflected solar radiation and emitted thermal radiation in 36 spectral channels, six of which are used to conduct aerosol retrievals (Levy et al., 2013; Remer et al., 2005, 2008). The 2,330 km swath of MODIS provides near global coverage. We use the combined quality controlled 550 nm AOD (dataset "Aerosol_Optical_Depth_Land_Ocean_Mean") from the collection 6.1 level 3 MODIS atmosphere daily global product (MxD08_D3; Levy et al., 2013; Wei et al., 2019). These level 3 data are gridded $1^o \times 1^o$ AODs obtained from the level 2 instantaneous products (Platnick et al., 2015). The dataset is built from the combined ocean (best) and land (corrected) retrievals which only contains AOD for filtered retrievals over dark targets. In particular, it includes Dark Target (Levy et al., 2013) ocean retrievals having quality assurance ≥ 1 and Dark Target land retrievals having quality assurance equal to 3.

We also use MODIS fine mode AOD (fAOD) from the same daily product. MODIS assumes nine tropospheric aerosol models with varying sizes (Levy et al., 2003). These include four fine modes (effective radii 0.10, 0.15, 0.20, and 0.25 μm) and five coarse modes: three for sea salt (effective radii 1.00, 1.50, 2.00 μm) and two for mineral dust (effective radii 1.50 and 2.50 μm).

MODIS fAOD is only included in collection 6.1 over the oceans and therefore the composites of fAOD shown are built from fewer points than those built from total AOD. The fAOD used in this study, dataset "Aerosol_Optical_Depth_Small_Ocean_Mean", is equal to the sum of the four fine modes. The remaining portion of the AOD is then contributed by coarse mode AOD (cAOD).

Prior to retrieving AOD, MODIS reflectances are cloud cleared at spatial resolution of 500 m. The cloud-free reflectances are averaged in 10 km × 10 km pixels if at least 10 out of 400 are available. Because of this, MODIS can retrieve AOD even if a 10 km scene is not entirely cloud free. Beginning with MODIS collection 6 this procedure uses an updated cloud masking routine to alleviate a known issue where AOD was a factor of two too large in scenes with cloud cover > 80% (Remer et al., 2008). We conduct additional filtering of the MODIS AOD and fAOD for any potential remaining cloud contamination by discarding $1^o \times 1^o$ grid cells with cloud coverage > 50%. Daily, this filtering results in the removal of about 60% of the global 1^o grid cells.

2.2 Reanalysis and Model Datasets

For identification of midlatitude cyclone centers we use sea-level pressure (SLP) from the NASA Modern Era Retrospective analysis for Research and Applications, version 2 (MERRA-2; Gelaro et al., 2017). MERRA-2 is the latest NASA reanalysis and is improved over its predecessor, MERRA, as a result of updates to the atmospheric general circulation model (Molod et al., 2015) and observing system (McCarty et al., 2016). MERRA-2 is output on a 0.5^o latitude × 0.625^o longitude (about 50 km on the cubed-sphere) grid and 72 vertical levels extending from the surface to the top of the atmosphere. The SLP field used to create the midlatitude cyclone database for this study comes from the MERRA-2 assimilated meteorology product (GMAO, 2015). We average the SLP from its original 3-hourly temporal resolution and use daily means.

The M2GMI simulation is a combination of the Goddard Earth Observing System (GEOS), version 5 general circulation model (Molod et al., 2015) and the Global Modeling Initiative chemistry mechanism (Duncan et al., 2007; Strahan, Duncan, & Hoor, 2007). It is constrained by MERRA-2 meteorology (winds, temperature, and pressure) through a replay technique (Orbe et al., 2017). The replay technique employed closely resembles the nudging approach described in

Kunz et al. (2011). M2GMI is output on the native MERRA-2 resolution ($0.5^o \times 0.625^o$, 72 vertical levels) and currently covers the period of 1980-2019. Fossil fuel and biofuel emissions in M2GMI come from the MACCity inventory (Granier et al., 2011) until 2010 while more recent years are scaled up following Representative Concentration Pathways (RCP 8.5) emissions. Full descriptions of the M2GMI simulation are provided in Nielsen et al. (2017) and Strode et al. (2019). M2GMI also includes a suite of idealized tracers. In this work, we use the 25-day anthropogenic carbon monoxide tracer (hereafter AnthroCO_{25d}). AnthroCO_{25d} has emissions corresponding to anthropogenic CO but undergoes decay at an idealized, fixed time of 25 days.

M2GMI is interactively coupled to the Goddard Chemistry and Aerosol Transport (GOCART) module for aerosols. GOCART simulates the major tropospheric aerosols of sulfate, black carbon, organic carbon, dust, and sea salt and was initially described by Chin et al. (2002) and Ginoux et al. (2001). Nitrate was added as described in Bian et al. (2017). A complete description of aerosol emissions and treatment in GOCART has more recently been given in Chin et al. (2009) and Colarco et al. (2010). Sea salt aerosol (SSA) emissions have been modified from the original Gong (2003) formulation by re-calibration to surface friction velocity and inclusion of a sea-surface temperature dependence (Jaeglé et al., 2011) as described in Randles et al. (2017). There are five size bins for SSA: 0.03-0.1, 0.1-0.5, 0.5-1.5, 1.5-5.0, and 5.0-10.0 μm. Dust emissions are a function of the surface characteristics and wind speed following Ginoux et al. (2001). Dust is also represented by five size bins: 0.1-1.0, 1.0-1.8, 1.8-3.0, 3.0-6.0, and 6.0-10.0 μm. Sulfate and carbonaceous species have primary emissions from fossil/bio- fuel combustion, biomass burning, as well as biogenic sources for organic carbon. Sulfate is also produced by oxidation of sulfur dioxide gas (SO_2) and dimethyl sulfide (DMS). Loss processes for each species include dry deposition (with gravitational settling), large-scale wet removal, and convective scavenging. To calculate precipitation-induced aerosol removal, a corrected precipitation product following Reichle et al. (2017) is used. We do note that while emissions in M2GMI are similar to those in the MERRA-2 aerosol reanalysis (Randles et al., 2017), M2GMI does not constrain total AOD through the assimilation of satellite AOD and thus serves as an independent dataset with which to probe aerosol export.

The original SSA emissions in M2GMI (8,934 Tg yr^{-1}, 2005-2018) are similar to those used in MERRA-2 (9,318 Tg yr^{-1}, 2000-2014; Randles et al., 2017), but more than a factor of 2 larger than the recent analysis of Bian et al. (2019) (4,016 Tg yr^{-1}) who used the NASA GEOS model with the GOCART module. The SSA GOCART emission scheme and meteorology are the same for these three simulations, however Bian et al. (2019) used a global scaling factor of 0.4, while MERRA-2 and M2GMI use a scaling factor of 0.875. Bian et al. (2019) showed good agreement of their simulations with comparisons to aircraft observations of aerosol mass concentrations as well as AOD from AERONET and MODIS. We thus scale SSA emissions, mass concentrations, and AOD in M2GMI by a factor of 0.46 (=0.4/0.875). The resulting SSA emissions are 4,060 Tg yr^{-1}, consistent with a number of the previous estimates reviewed in Weng et al. (2020). As aerosols are assumed to be externally mixed in GOCART, this scaling does not impact the other aerosol species simulated.

Aerosol optical properties in GOCART are from the Optical Properties of Aerosols and Clouds (OPAC; Hess, Koepke, & Schult, 1998; Koepke et al., 1997). Dust is assumed to be non-hygroscopic while the other species undergo varying degrees of growth at higher relative humidity (see Figure 2 in Chin et al., 2002). The AOD is calculated as $\tau = \beta M_d$, where β is the mass extinction efficiency (in m^2 g^{-1}) and M_d is the dry aerosol mass loading (in g m^{-2}). The mass extinction efficiency is a function of the aerosol refractive indices, size distribution, particle density, and relative humidity; it is assumed to be maximum at a relative humidity of 99%. Aerosol mass concentrations and AOD from GOCART simulations have been extensively validated against both ground-based and satellite observations (Chin et al., 2002, 2009, 2014; Colarco et al., 2010; Nowottnick et al., 2010).

To compare M2GMI against MODIS, the hourly M2GMI AOD and fAOD (sum of sulfate, organic carbon, black carbon as well SSA, dust, and nitrate with radii less than 1.0 μm) are linearly interpolated in time to 10 am or 2 pm local (i.e., near the Terra and Aqua equatorial crossing times). In addition, we sample daily-averaged aerosol properties from M2GMI. Finally, we sample daily-averaged meteorological fields from M2GMI in order to examine the WCB and broader midlatitude cyclone environment.

3. Methodology

Many recent analyses have utilized composites built from fields sampled in a cyclone-centered reference frame (e.g., Booth, Naud, & Jeyaratnam, 2018; Field & Wood, 2007; Grandey et al., 2011, 2013; McCoy et al., 2018; Naud et al., 2017, 2019). Although compositing hides the variability on a cyclone-by-cyclone basis, averaging across many cases enables common patterns associated with cyclone airstreams to emerge. Midlatitude cyclone composites in turn make it possible to study meteorological and chemical signatures, and their spatiotemporal variability, in a more general framework. Further, it provides a framework for testing whether these signatures are accurately captured by global models. The composites of Knowland, Doherty, & Hodges (2015) highlighted that the WCB of strong NH midlatitude cyclones tends to enhance carbon monoxide and deplete ozone in the middle and upper troposphere as it redistributes air from near the surface. Jaeglé et al. (2017) used cyclone-centered composites to validate modeled ozone against satellite observations before concluding that midlatitude cyclone DIs account for about half of all annual NH stratosphere-to-troposphere transport of ozone.

In this study, we use an approach that (1) identifies NH midlatitude cyclones; (2) samples satellite/model meteorological and aerosol fields on a 4,000 km × 4,000 km cyclone-centered grid; and (3) generates composites and examines anomalies relative to similarly sampled background conditions.

3.1 NH Midlatitude Cyclone Identification

We use the method described by Patoux, Yuan, & Li (2009) to identify NH midlatitude cyclone centers in the daily-averaged MERRA-2 SLP field. In brief, a cyclone center is identified if: (1) the grid cell is a true local pressure minimum (i.e., it is less than the eight surrounding cells); (2) the pressure is at least 1 hPa less than the pressure averaged over the surrounding grid cells up to ± 4 indices; (3) the Laplacian of pressure averaged over the same grid cells is at least 0.5×10^{-10} hPa m^{-2}. When two or more centers are identified within 2,000 km of each other, we only select the center with the lowest central SLP. Cyclone centers are also filtered for SLP ≤ 1,010 hPa to focus our analysis on mature cyclones most likely to have a coherent WCB airstream and therefore stronger transport. We note that our approach is conducted in a Eulerian framework and does not track the position of individual cyclones during their life cycle.

For the 2005-2018 period, we identify 27,707 midlatitude cyclones with centers poleward of 30° N. These midlatitude cyclones are relatively evenly distributed by season, with 29% of cyclones occurring in spring (March-April-May; MAM), 20% in summer (June-July-August; JJA), 25% in fall (September-October-November; SON), and 26% in winter (December-January-February; DJF). The spatial distribution of the annual mean midlatitude cyclone occurrence frequency is given in Figure 1. The shading represents fraction of days for 2005-2018 that a point is within a midlatitude cyclone. To generate this frequency, we calculate the size of each cyclone as defined in Patoux, Yuan, & Li (2009). Consistent with numerous previous studies, cyclones occur most frequently (on > 12% of days) in the North Atlantic and North Pacific storm tracks (e.g., Hoskins & Hodges, 2002; Ulbrich, Leckebusch, & Pinto, 2009; Wernli & Schwierz, 2006). While most cyclones occur over the NH oceans, there are regions over land in both North America and Asia where the cyclone frequency is > 4%. The frequency map also captures two regions of climatological low-pressure (i.e., high cyclone frequency) in the Gulf of Alaska and off the coast of Iceland.

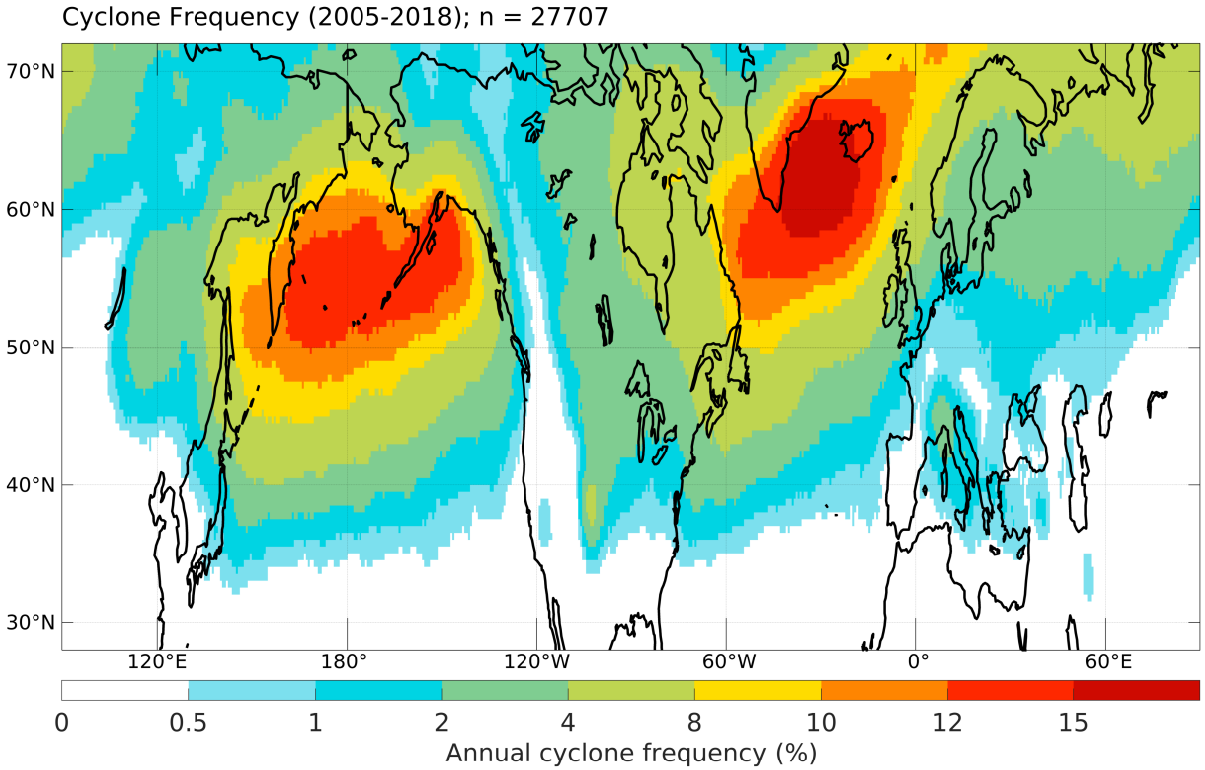

Figure 1. Annual mean NH midlatitude cyclone occurrence frequency for 2005-2018.

3.2 Sampling and Compositing Approach

We conduct cyclone-centered sampling of the MODIS and M2GMI fields at a resolution of 1°. For M2GMI, we first regrid the fields from the native 0.5° × 0.625° grid to the 1° × 1° MODIS grid. For each cyclone we follow the methods of Field & Wood (2007) by using bilinear interpolation to translate and regrid the daily-averaged fields onto a 4,000 km × 4,000 km region centered over the cyclone. Our cyclone-centered grid has 100 km horizontal grid spacing. We then average together the cyclones to generate annual and seasonal composites. For comparison to MODIS, the 10 am and 2 pm local time M2GMI AOD fields are only sampled when there are valid 1° × 1° MODIS retrievals and MODIS cloud fraction < 50%. The same approach is also applied to 24-hour daily mean M2GMI meteorological and aerosol fields without any sampling.

To examine how each midlatitude cyclone perturbs the distribution of aerosols relative to background conditions we generate a separate cyclone-centered grid at the same date and location of the original cyclone but instead using a 60-day running mean of each field smoothed with a 6° wide boxcar average. Anomalies (e.g., ΔAOD) are given as the difference between the cyclone and its background ($\Delta AOD = AOD_{cyclone} - AOD_{background}$) or as the percent enhancement relative to background ($\Delta AOD = 100 \times (AOD_{cyclone} - AOD_{background}) / AOD_{background}$, in %).

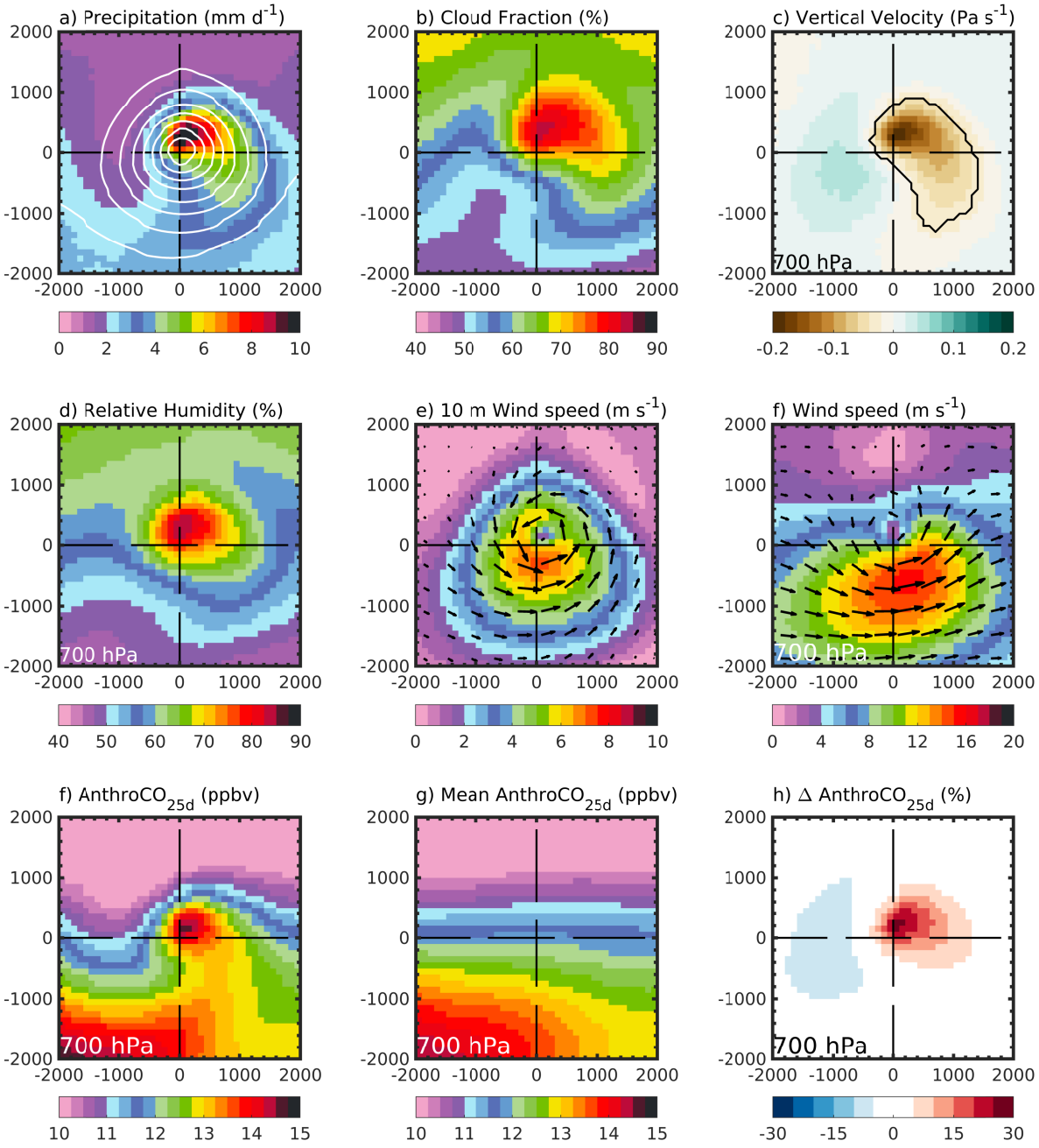

Figure 2. Annual mean composites of 27,707 midlatitude cyclones from M2GMI (2005-2018). (a) Precipitation (mm d^{-1}), with sea-level pressure contours in white; (b) total cloud fraction (%); (c) 700 hPa vertical velocity (Pa s^{-1}); (d) 700 hPa relative humidity (%); (e) 10 m wind speed (m s^{-1}), with vector winds represented by arrows; (f) 700 hPa wind speed (m s^{-1}), with vector winds represented by arrows; (f) 700 hPa $AnthroCO_{25d}$ (ppb); (g) Background 700 hPa $AnthroCO_{25d}$ (ppb); (h) 700 hPa $AnthroCO_{25d}$ anomaly. For each panel, the *x* and *y* axes labels represent the distance from the cyclone center ($x = 0$ and $y = 0$) in kilometers, with *x* increasing in the eastward direction and *y* increasing in the poleward direction.

Figure 2 shows the annual mean 2005-2018 NH midlatitude cyclone composites of M2GMI precipitation, cloud fraction, vertical velocity (ω) at 700 hPa, relative humidity (RH) at 700 hPa, 10 m wind speed, and wind speed at 700 hPa. Maximum precipitation (> 8 mm d^{-1}) occurs near the center of the cyclone and curves to the southwest to create the characteristic comma shape (e.g., Field & Wood, 2007; Naud et al., 2017; Figure 2a). Strongest ascent (minimum ω) associated with the WCB also occurs near the center of the cyclone co-located with the region of precipitation. Vertical velocity values of -0.2 hPa s^{-1} in this region of the composite represent about 175 hPa of overall ascent extrapolated to a 24-hour period (Figure 2c). The most extensive cloud cover (> 75%) in the composite occurs where the WCB turns cyclonically and creates the "cloud head" as viewed in satellite imagery (Catto et al., 2010; Figure 2b). The air at 700 hPa has high relative humidity (> 80%) near the center of the composite (Figure 2d). The flow near the surface at 10 m is cyclonic around the center of the cyclone, with wind speeds as high as 7 m s^{-1} just to its south (Figure 2e). At 700 hPa the cyclonic flow is offset from the surface low by about 200 km to the northwest. In the southern half of the domain, the 700 hPa flow is out of the west southwest and wind speeds reach as high as 18 m s^{-1} (Figure 2f).

Figures 2f-h show the composites of 700 hPa (i.e., lower free troposphere) AnthroCO_{25d} from M2GMI. Both the cyclone and background composites display the largest concentrations of AnthroCO_{25d} (15-16 ppbv) in the southwest of the domain, reflecting outflow from the polluted continental boundary layer. The cyclone composite also shows that as the WCB ascends and wraps into the cyclone center, it carries elevated AnthroCO_{25d} (13-15 ppbv) offshore and into the free troposphere (Figure 2f). This also serves to disrupt the latitudinal gradient of AnthroCO_{25d} found in the background composite (Figure 2g). The ΔAnthroCO_{25d} composite highlights that cyclone WCBs on the whole export polluted air masses and can enhance mean AnthroCO_{25d} in the lower free troposphere by 15-30% compared to background conditions (Figure 2h). The composites also display a 5-10 % reduction in AnthroCO_{25d} behind the cyclone as cleaner air is transported equatorward both from higher altitude and latitudes in the DI.

4. Aerosol Optical Depth Composites

4.1 Total and Fine Mode Aerosol Optical Depth Composites from MODIS and M2GMI

Figure 3 shows composites of AOD and fAOD from MODIS Aqua and M2GMI. The composites exhibit a pattern of elevated AOD to the east of the cyclone center in the WCB, with values of

0.13-0.16. Maximum AOD in the WCB is found within 1,000 km of the cyclone center and curves to the southwest with the characteristic comma-shape. This coincides with the regions of precipitation and cloud cover seen in Figure 2. M2GMI predicts slightly higher values of 0.14-0.18, and captures the cyclone-wide features observed by MODIS quite well ($r = 0.88$; Figures 3a-d). The AOD anomalies display positive enhancements of 20-45% (30-50%) above background seen in MODIS (M2GMI). MODIS and M2GMI show similar decreases (-25%) in AOD to the west of the cyclone center the DI, reflecting transport of cleaner air from higher latitudes and altitudes (Figures 3a-d).

MODIS fAOD reaches values of 0.07-0.09 to the east and northeast of the cyclone center (Figure 3e). In this region M2GMI captures similar values of fAOD (0.07-0.1) but across a larger area that is spread out to the east (Figure 3g). For both MODIS and M2GMI, the fine mode fraction (FMF; calculated as fAOD / AOD) displays values of 0.5-0.6 in the WCB. This is consistent with the findings of Naud et al. (2016) who found the breakdown of MODIS fine and coarse AOD to be about equal in the warm sector. Also consistent with their work, behind the cyclone in the cold sector fAOD can reach as high as 0.07 (FMF = 0.9; Figures 3e,g).

In the WCB, both MODIS and M2GMI show fAOD enhancements of 20-40% relative to background fAOD (Figures 3f,h) that accounts for 68% of the annual AOD enhancements to the east and northeast of the cyclone center. In addition, both datasets show that cAOD is maximum (> 0.08) near the center of the composite, where it is enhanced by more than a factor of two relative to background cAOD (Figures 3i-l).

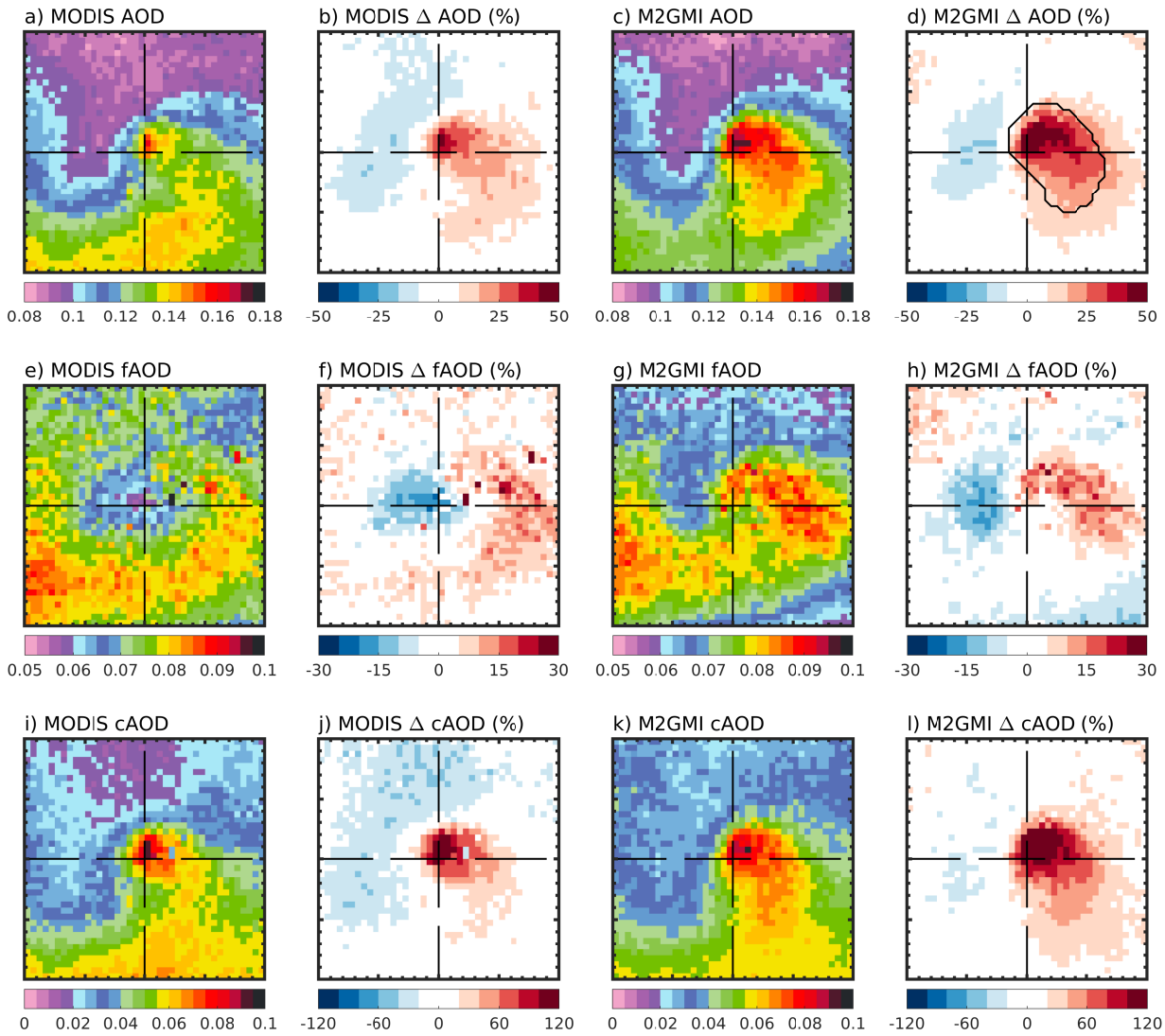

Figure 3. Midlatitude cyclone composites of AOD, fine AOD (fAOD), coarse AOD (cAOD), and their enhancements for MODIS Aqua (a, b, e, f, i, and j) and M2GMI (c, d, g, h, k, and l). Enhancements are given in as a percent relative to the respective backgrounds. The M2GMI AOD is sampled at the Aqua overpass time only when there are valid MODIS AOD observations (section 3.2). The black contour in Figure 3d corresponds to the warm conveyor belt region as defined in section 4.1. The composites shown represent the same cyclones shown in Figures 1 and 2.

The composites shown in Figure 3 have some remaining noise artifacts in both MODIS and the sampled M2GMI. This is due to the combination of two things. First, because the cyclone environment is inherently cloudy (Figure 2b), and because we impose additional cloud filtering onto the MODIS AOD, the composites reflect the mostly cloud-free grid cells within the cyclone. In addition, the MODIS fAOD is only available over the oceans and so there are inherently fewer points in the fAOD and cAOD composites. Regardless, we find that roughly

80% of the midlatitude cyclone cases have valid data for fAOD and the composites in Figure 3 do not change considerably if only examining cyclones over the NH oceans. Annual mean composites for MODIS Aqua and Terra reflecting the number of cyclones with valid data for total and fAOD/cAOD are shown in Figure S1.

For each cyclone, we identify the WCB as the outermost closed 700 hPa ω contour enclosing an ω minimum (ascent maximum) within 1,000 km of the cyclone center. The black contour in Figure 3d shows the area of the WCB when the identification procedure is carried out on the vertical velocity composite from Figure 2c. We calculate the mean AOD in the WCB region of each cyclone and the resulting seasonal cycle in MODIS and M2GMI AOD is shown in Figure 4. The WCB AOD observed by MODIS reaches its maximum in April and May, with a secondary maximum in July. M2GMI reproduces the observed MODIS AOD well ($r = 0.97$; NMB = 5.9%). When expressed as an enhancement relative to background ($\Delta AOD = 100 \times (AOD_{cyclone} - AOD_{background}) / AOD_{background}$) we find that MODIS AOD is enhanced by 65-69% on average, with the highest enhancements occurring in July (90%) when background AOD is at a minimum. Note that extracting AOD values within individual WCBs yields values larger than seen in the Figure 3 composites as application of the identification criteria to each cyclone individually allows the location of the WCB to vary. Overall, we find that fAOD accounts for two-thirds of the AOD enhancement in cyclone WCBs annually, thus suggesting that fine aerosols make up a large fraction of the AOD in cyclone WCBs. When comparing M2GMI to MODIS Terra composites, we find similar results, with MODIS Terra being slightly larger than Aqua (e.g., Wei et al., 2019; Figure S2-3).

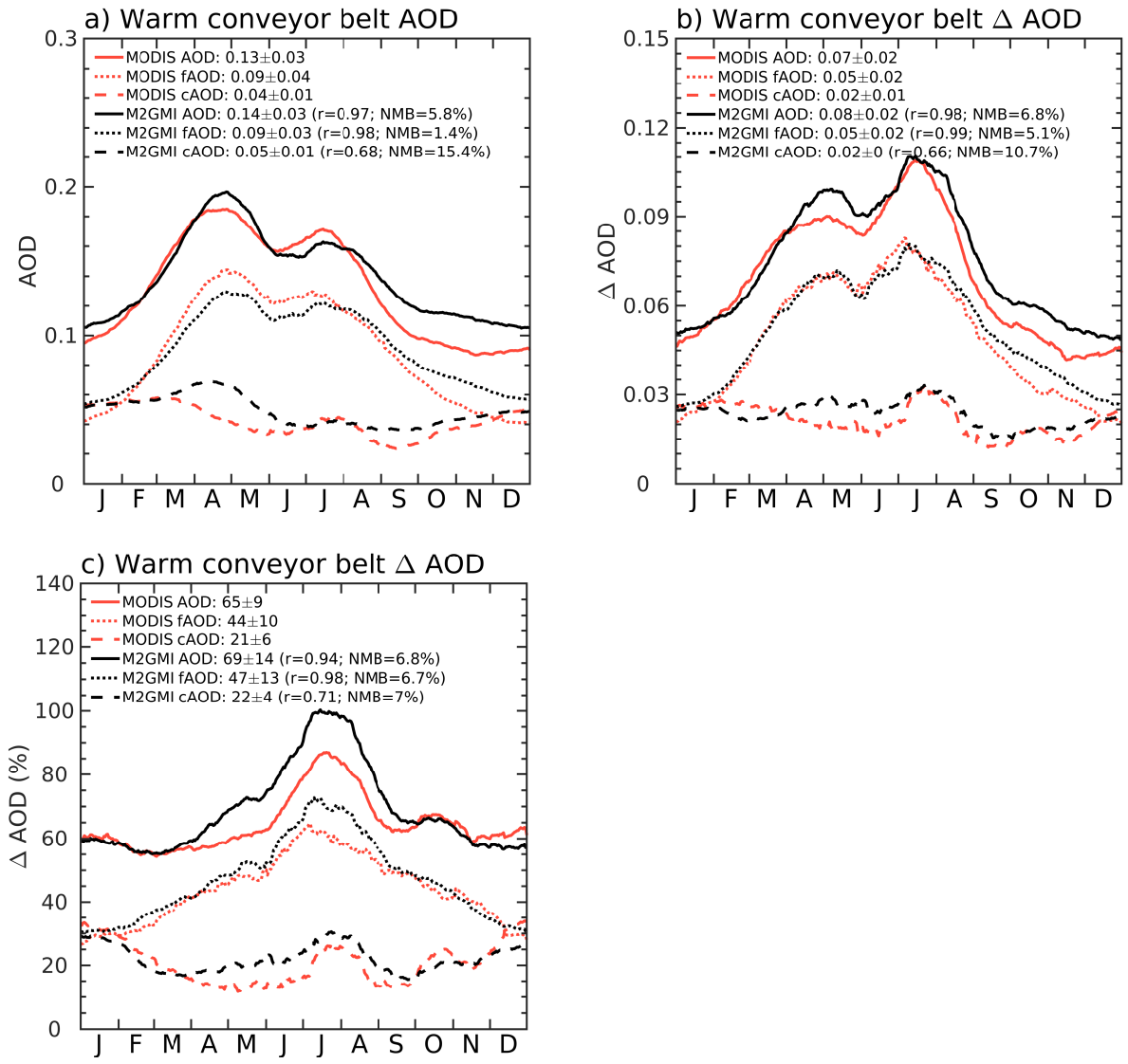

Figure 4. (a) Composite seasonal cycle for AOD, fAOD, and cAOD in the warm conveyor belt of individual cyclones (section 4.1). (b) Composite seasonal cycle for AOD, fAOD, and cAOD anomalies. (c) Same as (b) but expressed a percent relative to the total AOD background. Values are shown for MODIS Aqua (orange lines) and M2GMI (black lines). A 40-day boxcar smoothing has been applied to each time series. Annual mean values for each timeseries are also given in the legend.

4.2 Contributions of individual aerosol species to AOD in midlatitude cyclones

We now use M2GMI to examine the contribution of individual aerosol species to the AOD composites (Figure 5). For the composites in Figure 5, we use daily mean M2GMI values instead of the 10 am Aqua overpass time, and do not apply any sampling relative to MODIS data availability. Like the composites shown in Figure 3, the WCB stands out as a region of large AOD (> 0.2) to the east of the cyclone center. Overall, the total AOD composite in Figure 5a

displays values that are 25-30 % larger than those in Figure 3c due to the cloud filtering mentioned above.

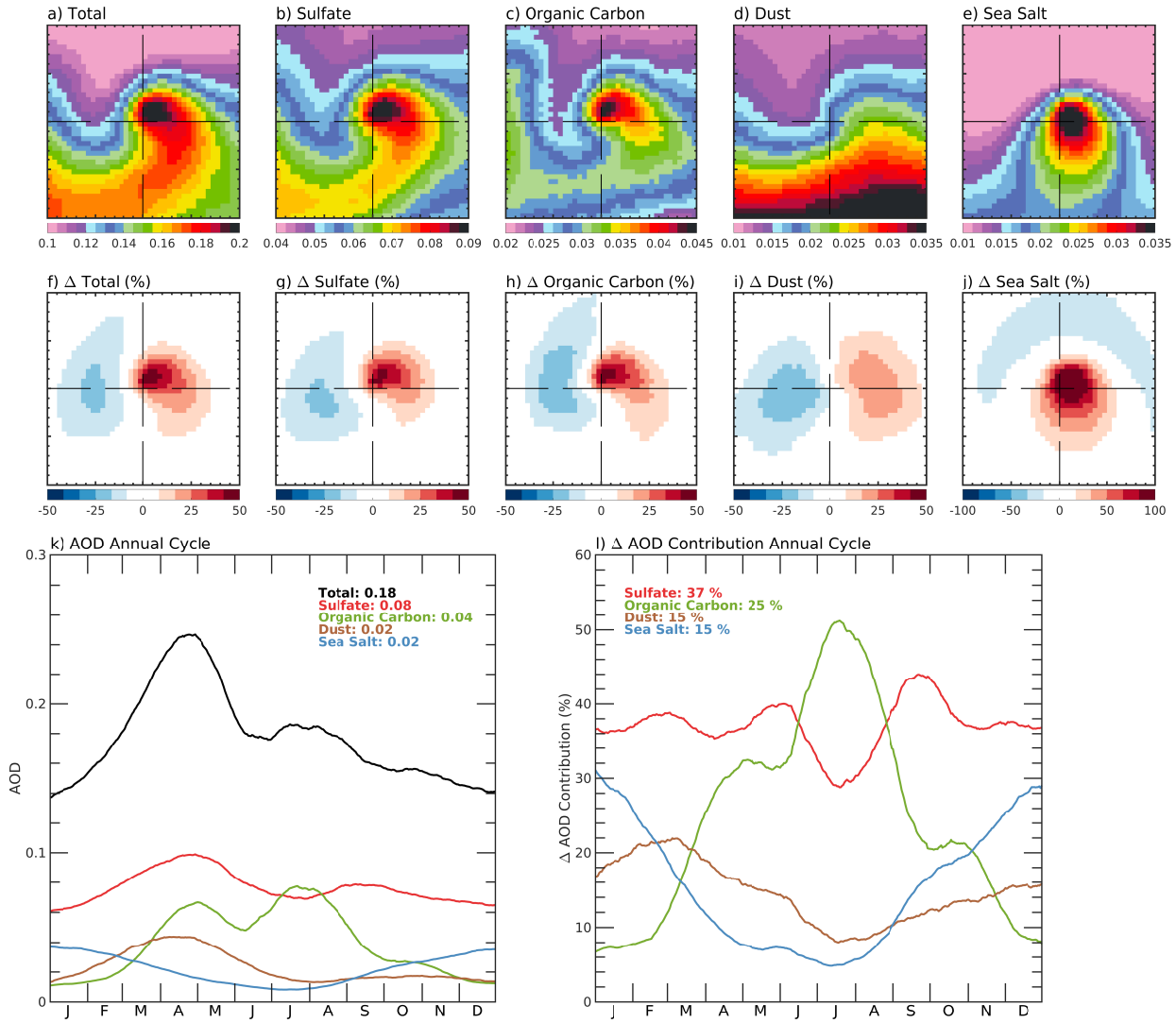

Figure 5. Top row: midlatitude cyclone composites of M2GMI AOD for total AOD (a), sulfate (b), organic carbon (c), dust (d), and sea salt (e). Middle row: Same as top row but expressed as anomalies relative to background values. For individual aerosol species, the background is defined relative to that species (i.e., $\Delta AOD_{dust} = 100 \times (AOD_{dust} - AOD_{dust,\ background}) / AOD_{dust,\ background}$). Bottom row: Annual cycle of M2GMI total and per species AOD in the WCB of midlatitude cyclones (k). The timeseries have been smoothed with a 40-day boxcar average and annual mean values for each species are given in the legend. (l) Same as (k) but for the contribution of each species to the total AOD enhancements in individual cyclones.

The individual component composites in Figure 5 show that sulfate accounts for 35% of the total AOD near the center of the composites, with organic carbon and SSA each accounting for another 15-20%. Sulfate and organic carbon show enhancements of 20-50% in the WCB region

while SSA AODs are more than doubled near the center of the composite. Dust enhancements maximize at 30% in a region spread out to the east of the cyclone center (Figure 5g-j). We do not show the composites for black carbon and nitrate as, combined, we find they contribute < 10% of the AOD. The seasonality of total AOD shows a strong spring maximum, similar to Figure 4a. The spring maximum in total AOD is driven by maxima in sulfate, organic carbon, and dust, which respectively contribute 38%, 33%, and 20% of the ΔAOD at this time (Figure 5k-l). The AOD annual cycles likely stem from a combination of seasonal variations in WCB strength and source region (Madonna et al., 2014) and the cyclone environment allowing for differential production and removal (Field and Wood, 2007; Chang and Song, 2006) during different times of the year. SSA AOD displays a strong seasonality that is maximum in winter and minimum in summer due to reduced cyclone strength in summer (Field and Wood, 2007) leading to less activity at the ocean surface. Overall, we find that annually, sulfate and organic carbon together constitute 62% of the ΔAOD in midlatitude cyclones.

4.3 Variability of AOD Enhancements in Cyclone WCBs

The composites shown in Figures 3-5 show that, on average, AOD in the WCB of midlatitude cyclones is enhanced by 30-50%. However, compositing hides much of the cyclone-to-cyclone variability which arises from whether air in the WCB originates from the continental boundary layer, with various degrees of pollution, or from the clean marine boundary layer. Figure S4 summarizes this variability and shows the cumulative distribution (CDF) of ΔAOD for individual aerosol components from the M2GMI simulation. Annually, we find that 74% of NH cyclones display enhanced total AOD in their WCBs, with 45% of cyclones having AOD enhancements of more than 20% and with 11% of cyclones having AOD enhancements exceeding 50 % (Figure S4). Conversely, only 26% of NH midlatitude cyclones have a WCB AOD lower than background conditions. These cyclones are predominantly over open ocean near the end of their life cycle (e.g., in the Gulf of Alaska and off the coast of Iceland). This means the WCBs of these cyclones are drawing fresh air from cleaner regions and any enhancements in aerosol would likely have been removed during precipitation earlier in the storm's lifecycle. Organic carbon and SSA ΔAOD follow a steeper distribution than sulfate (with a larger number of cyclones displaying larger enhancements) because of their stronger seasonality relative to sulfate.

Dust export in cyclone WCBs appears much more episodic, with only 39% of all cyclones showing enhancements in dust AOD (Figure S4).

Figure 6 examines variability in total AOD by storm track region from MODIS and the sampled M2GMI simulation. For the 2005-2018 period our database contains 11,140 midlatitude cyclone centers in the North Pacific (>30° N, 110°E – 120°W) and 8,724 cyclones in the North Atlantic (>30°N, -90°E – 20°E). Cyclones in the North Pacific have AODs > 0.12, maximizing at 0.17-0.18 in the WCB region, that correspond to enhancements of up to 40% (Figure 6e-f). Conversely, cyclone WCBs in the North Atlantic have AODs that maximize at 0.11 (Figure 6c-d). Nevertheless, due to the reduced background AOD (not shown), midlatitude cyclones in the North Atlantic storm track also enhance AOD by up to 35% (Figure 6g-h). Overall, Figure 6 suggests that the more polluted upwind continent leads to 60% larger AODs in North Pacific WCBs.

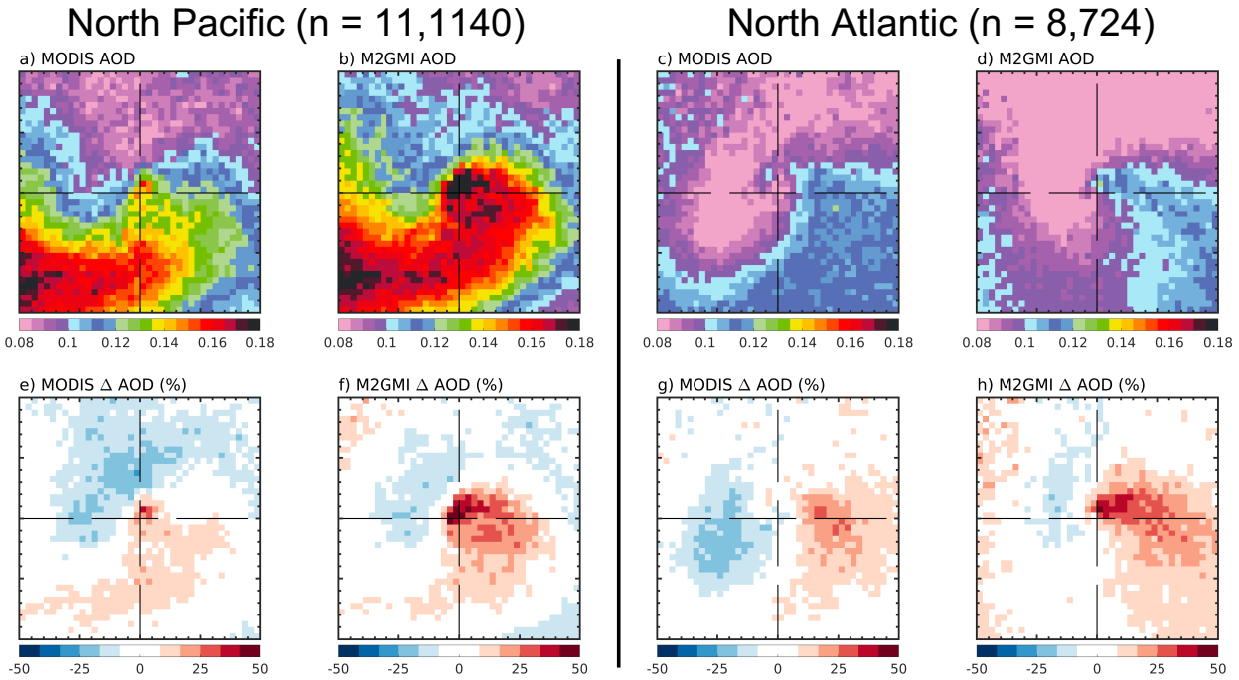

Figure 6. Midlatitude cyclone composites of AOD and its enhancement for cyclones in the North Pacific (a, b, e, f) and North Atlantic (c, d, g, h) storm tracks. The storm track bounds are given in section 4.3 of the text. Composites are given for MODIS Aqua and M2GMI. The M2GMI AOD is sampled at the Aqua overpass time only when there are valid MODIS AOD observations (section 3.2).

To further characterize storm track variability in AOD we examined the relationship between WCB AOD and 700 hPa $\Delta AnthroCO_{25d}$. Here, $AnthroCO_{25d}$ serves as a proxy for pollution. We grouped cyclone WCBs in 5% $\Delta AnthroCO_{25d}$ bins. In the North Pacific storm track total AOD shows a strong correlation with WCB pollution levels, nearly doubling from 0.11 (0.12) to 0.19 (0.21) in MODIS (M2GMI). This relationship is weaker for North Atlantic cyclone WCBs. Examining the same relationships for fAOD (Figure 7b) and cAOD (Figure 7c) reveals that most of the increase in AOD with increasing pollution is due to increases in fAOD. In WCBs with negative $\Delta AnthroCO_{25d}$ fAOD constitutes just over half of the AOD whereas for cyclones with large $\Delta AnthroCO_{25d}$ it constitutes nearly 80% (Figure 7a-b).

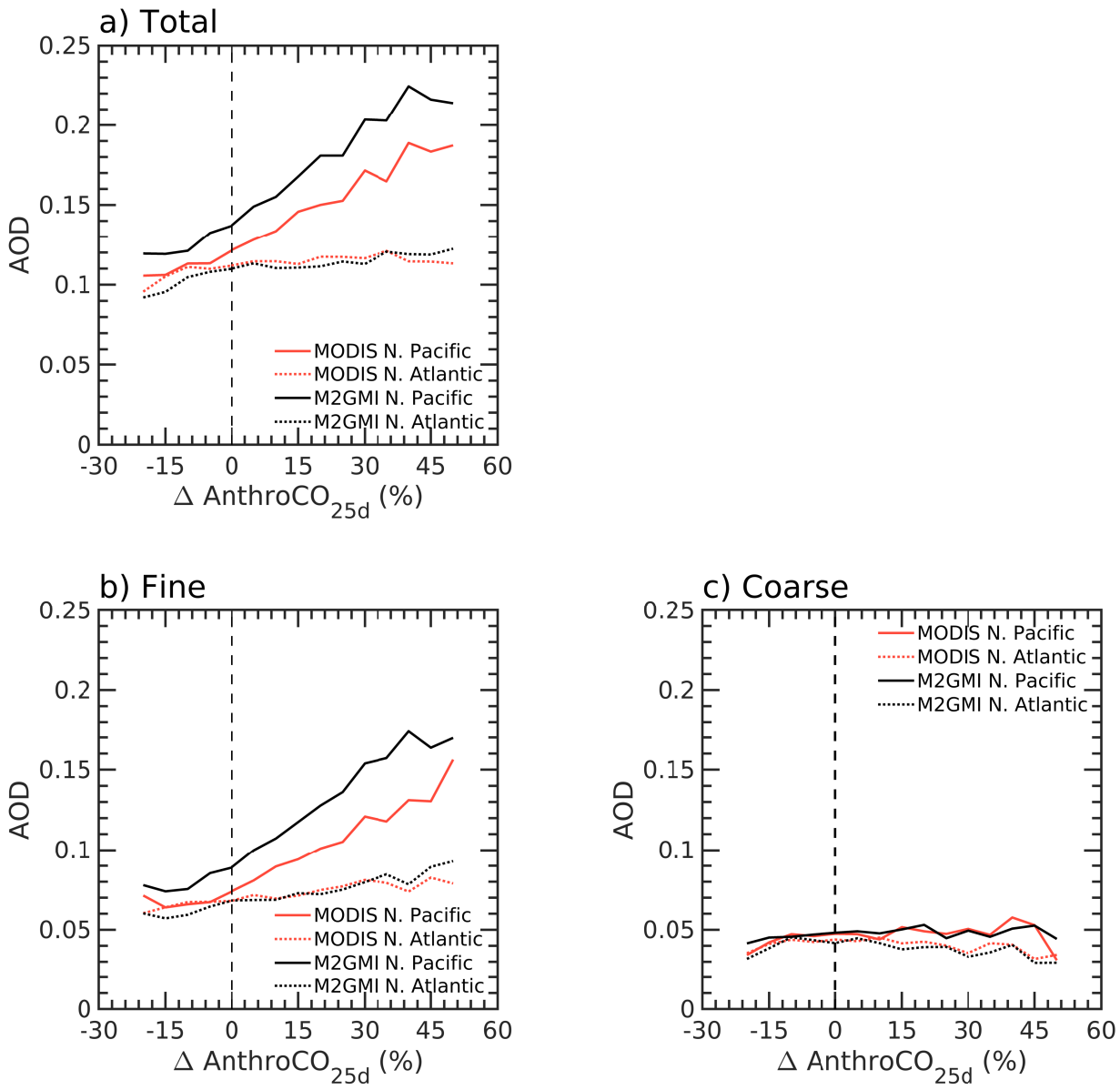

Figure 7. Relationship between anthropogenic pollution and total, fine, and coarse AOD in the warm conveyor belt of individual cyclones (section 4.1). Cyclones have been grouped in 5% bins based on M2GMI ΔAnthroCO$_{25d}$. The relationships are given for MODIS Aqua (orange lines) and M2GMI (black lines) corresponding to the North Pacific (solid lines) and North Atlantic (dashed lines) storm tracks. The M2GMI AOD is sampled at the Aqua overpass time only when there are valid MODIS AOD observations (section 3.2).

Based on the component AOD relationships we find that sulfate explains most of the AOD and fAOD differences between storm tracks (Figure S5). We also find stronger organic carbon and dust relationships with pollution in North Pacific cyclones (Figure S5). The latter is consistent with the picture of dust export off the Asian continent reported in previous studies (Huebert et

al., 2003; Uno et al., 2008). SSA displays behavior opposite to that of the continental aerosols, with a small decrease in AOD as $\Delta AnthroCO_{25d}$ increases. This behavior is similar in both storm tracks. Together, these opposite relationships with pollution lead to no relationship with overall cAOD and pollution (Figure 7c). M2GMI captures the magnitude and strength of the observed relationships quite well with a consistent 0.02 overestimate in AOD and fAOD (Figure 7).

5. Vertical Distribution of Aerosol Extinction and Mass

Figure 8 shows the layer-mean composites of M2GMI total aerosol extinction, aerosol extinction enhancement, dry mass enhancement, vertical velocity, and RH between the surface and 8km. To calculate the overall dry mass enhancement, the individual component dry mass enhancements have been weighted by their contribution to the background AOD in M2GMI. To the east of the cyclone center in the WCB, the composites demonstrate that aerosol extinction is enhanced by more than 20-40% through a deep layer extending from the surface to 8 km (Figure 8). This enhancement in extinction coincides with strong upward motion and high RH. Negative extinction anomalies correlated with transport of cleaner air are found to the west of the cyclone center in the DI. Below 1 km, the extinction enhancements reach up to 90% near the center of the cyclone. Near the surface, dry aerosol mass enhancements are on the same order as extinction enhancements. As the WCB ascends above 1-2 km, it begins to spread out to the east and northeast, wrapping cyclonically with the DI into the center of the cyclone (Figure 8). This is indicative of our selection of midlatitude cyclones being dominated by stronger, cut-off cyclones (Whitaker et al., 1988). As the WCB ascends, the magnitude of dry mass enhancements decrease more quickly than extinction enhancements. For example, in the 5-8 km layer extinction enhancements maximize at 20% while dry mass enhancements are only 10-12% (Figure 8). Negative extinction anomalies correlated with transport of cleaner air are found to the west of the cyclone center in the DI.

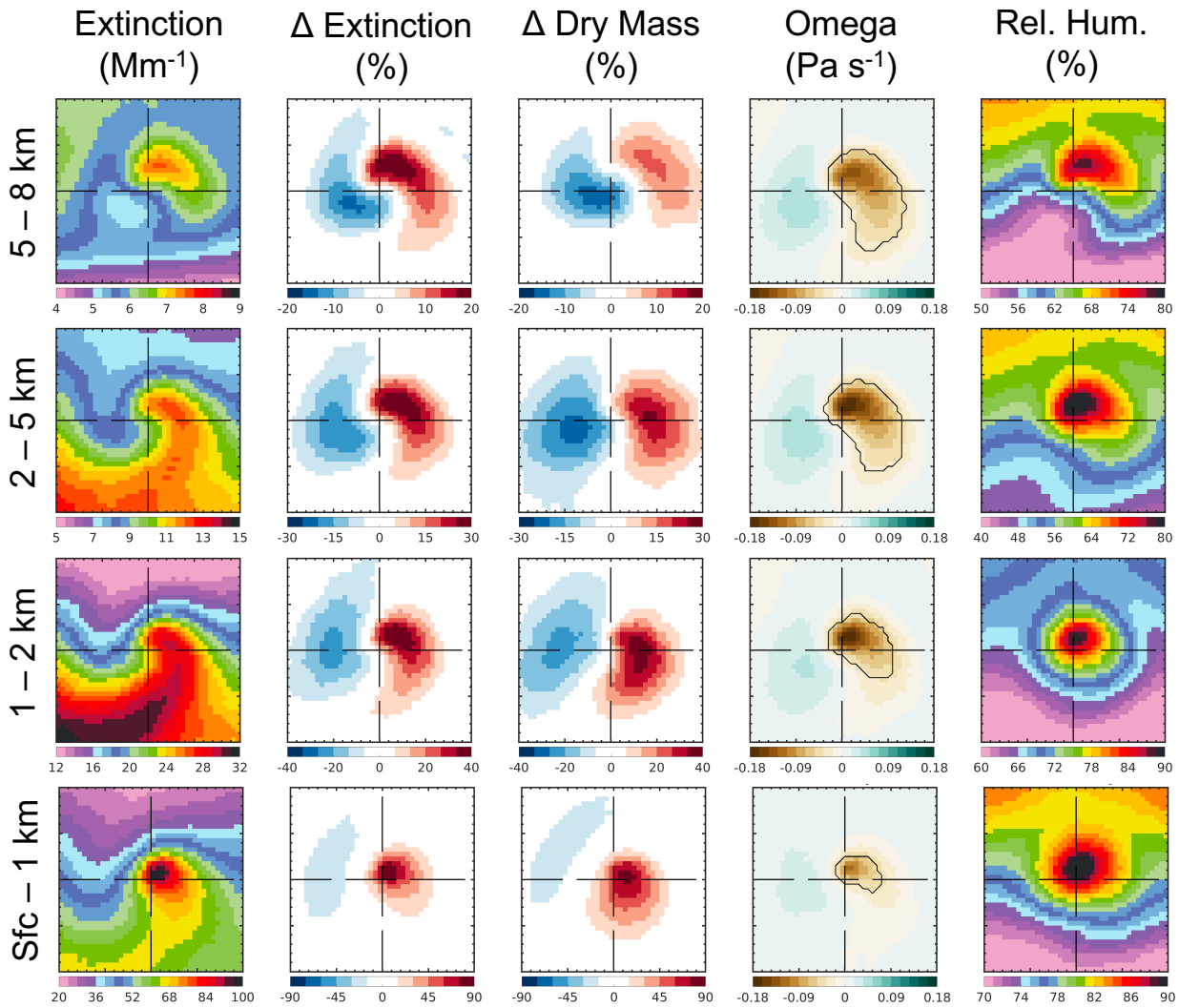

Figure 8. Composites of M2GMI layer mean total aerosol extinction (first column; Mm^{-1}), Δ extinction (second column; %), Δ dry mass (third column; %), vertical velocity (fourth column; Pa s^{-1}), and relative humidity (fifth column, %) for 2005-2018 NH midlatitude cyclones. The Δ dry mass has been weighted according to each aerosol component's contribution to the background extinction (section 5). The altitude layers correspond to 5-8 km (top row), 2-5 km (second row), 1-2 km (third row), and 0-1 km (bottom row). The black contours in the third column represent the average extent of the warm conveyor belt airstream (as defined in section 4.1 of the text).

Figure 9a shows the annual mean extinction profile within the WCB, identified using the vertical velocity field at each altitude (as in section 4.1). Below 1 km in altitude, the extinction is dominated by sulfate and SSA, which together account for nearly three-quarters of the 70% enhancement in total extinction (Figure 9b). SSA extinction rapidly declines away from the surface, reaching a third of its surface value by 0.75 km in altitude. Sulfate is the largest contributor to extinction throughout much of the profile and contributes > 40% of the extinction

enhancement in the 1.5-4 km layer. Export of organic carbon also occurs at higher altitudes where it contributes > 30% of the extinction enhancement above 4 km (Figure 9b). These results are consistent with Luan & Jaeglé (2013), who found sulfate export to occur at altitudes between 1-3 km and 2-6 km off of North America and Asia, respectively. They are also consistent with He et al. (2012) who noted elevated concentrations of sulfate precursors in the free troposphere between 2-4 km over China in spring. The contribution of dust to the total extinction enhancement maximizes at > 20% in the free troposphere between 2.5-5.5 km. While dust particles may be lifted in the WCB, much of the signature in the profiles likely comes from horizontal export of dust from high altitude desert regions in Asia (e.g., Eguchi et al., 2009; Huang et al., 2008). The altitude of dust export shown in the Figure 9 profiles are also consistent with the 2.5-4 km altitude seen in the springtime case study presented in Uno et al. (2008).

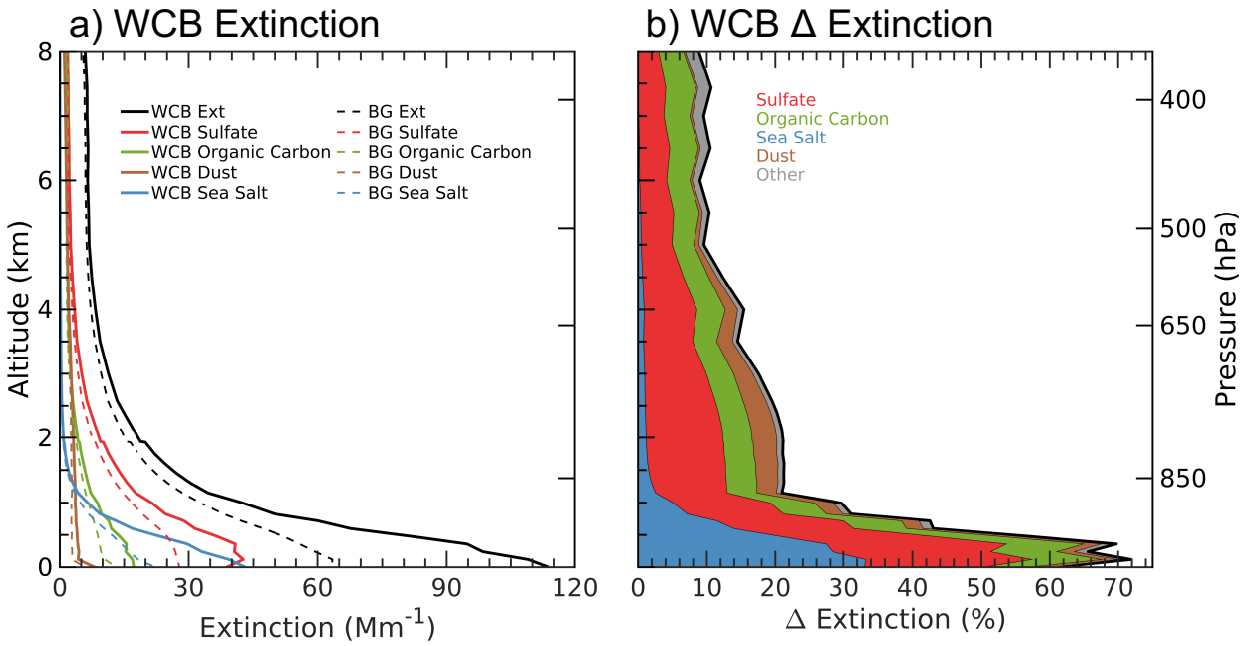

Figure 9. Annual mean vertical profiles of M2GMI aerosol extinction (units of Mm^{-1}) in the WCB of midlatitude cyclones. (a) Absolute extinction values (solid lines), and background extinction values (dashed lines). Resulting column AOD values for the cyclone profiles are given in the legend. (b) Extinction enhancement given as a percent relative to the total background. The individual component (colored) lines add together to the total extinction enhancement (black line).

How much of the enhanced AOD in the WCB is due to humidification as opposed to increased aerosol mass? To first order, enhancements in aerosol extinction are equal to the sum of enhancements in dry mass and mass extinction efficiency. As mentioned in section 2.2, all

aerosol growth due to relative humidity is included in the mass extinction efficiency (β). Overall, we find that while total AOD enhancements are 20-50% in the WCB, column mass enhancements are only 10-25% (Figure S6). Thus, aerosol growth by humidification accounts for up to half of the ΔAOD in cyclone WCBs. We find this contribution varies between 20% for SSA, which occurs in the already humid marine boundary layer, to 50-60% for sulfate and organic carbon, which are exported to higher altitudes where humidification plays a larger role. These conclusions are consistent with the layer mean extinction and mass enhancement composites shown in Figure 8.

6. Midlatitude Cyclone Sea Salt Aerosol Emissions and Net Effect on NH Aerosols

6.1 Sea Salt Aerosol Emissions

We now examine the contribution of midlatitude cyclones to enhancing SSA emissions. Figure 10a shows the M2GMI mean composite of SSA emissions for all NH midlatitude cyclones in 2005-2018. A core of large emissions (> 40 kg km^{-2} d^{-1}) occurs approximately 100-500 km south of the cyclone center. We calculate total SSA emissions in the high wind speed region (u_{10m} > 5 m s^{-1}) within 2,000 km of the cyclone center for the composite and find that, on average, NH midlatitude cyclone lead to SSA emissions of 0.179 Tg d^{-1}. Annually, this results in 355 Tg yr^{-1}, compared to the total SSA emissions of 594 Tg yr^{-1} in the 30–80° N region (Figure 10b). Thus, midlatitude cyclones account for 60% of the total SSA emissions.

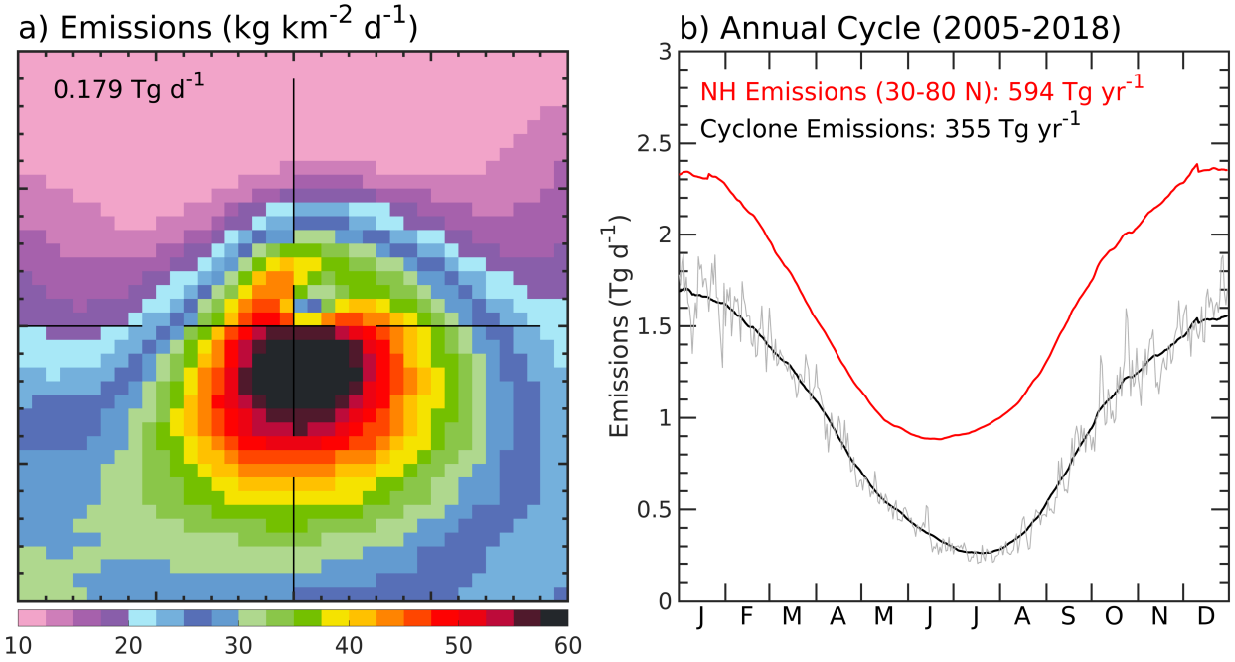

Figure 10. (a) Cyclone composite of SSA emissions (kg km^2 d^{-1}). The mean daily composite emissions calculated as in section 6.1 is given in the top left of the panel. (b) Annual cycle of NH midlatitude cyclone sea salt emissions (daily emissions are in gray while the black line shows emissions smoothed with a 40-day boxcar average). The multiyear mean 30-80 ° N emissions are shown in red.

We apply the same approach as above to calculate SSA emissions for individual midlatitude cyclones and show the resulting annual cycle in Figure 10b. SSA emissions from midlatitude cyclones maximize in winter (1.5-1.8 Tg d^{-1}) and decrease to a summer minimum of 0.3-0.5 Tg d^{-1}. This seasonal variability follows from the seasonal variability in u_{10m} (Figure S7). As noted above, midlatitude cyclones account for 60% of the total SSA emissions between 30–80° N. The region of high winds over which we integrate SSA emissions covers 40% of the NH ocean area annually (Figure S7). Therefore, midlatitude cyclones account for more than twice as much SSA emissions per surface area as the rest of the NH oceans.

6.2 Net effect of Midlatitude Cyclones on NH Aerosol Budgets

We combine daily-averaged aerosol processes from M2GMI using a budget approach to examine the complete picture of aerosol formation, removal, and transport within NH midlatitude cyclone WCBs. Figure 11 provides an example of this approach for sulfate across all NH cyclones. Cyclone-centered and enhancement composites are shown for column integrated direct emissions, chemical production, loss via dry and deposition, horizontal flux, and burden. Primary

sulfate emissions are minimal and not associated with cyclone WCBs. Production of sulfate maximizes at 2-3 kg km^{-2} d^{-1} to the northeast of the cyclone center (Figure 11b) and is driven primarily (> 80%) by aqueous oxidation of SO_2 in the cloudy WCB environment. Loss of sulfate in the WCB (> 4 kg km^{-2} d^{-1}; Figure 11c) is driven by wet deposition from largescale precipitation in the WCB. Advective fluxes of sulfate are large in the WCB (> 3 kg km^{-2} d^{-1}; Figure 11d) but overall do not fully balance depositional losses. This suggests export of sulfate follows the conceptual models put forth in Brock et al. (2004) and Dunlea et al. (2009). Cyclone WCBs efficiently scavenge all transported sulfate aerosol and most enhancements in sulfate mass (0.5-1 kg km^{-2} d^{-1}; Figure 11j) are due to chemical production in the WCB.

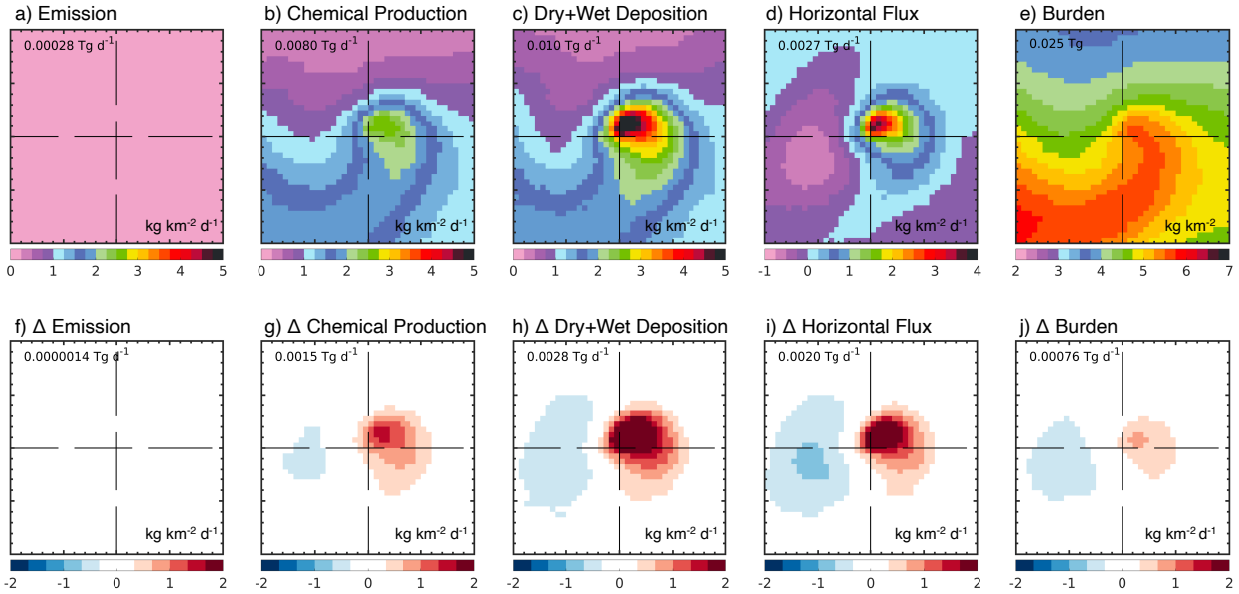

Figure 11. The sulfate mass balance within northern hemisphere midlatitude cyclones. (a-e) Cyclone composites of (a) emissions, (b) chemical production, (c) dry and wet deposition, (d) horizontal flux (all units of kg km^{-2} d^{-1}), and (e) burden (units of kg km^{-2}). (f-j) Cyclone composites of mass balance enhancements (units of kg km^{-2} d^{-1}), highlighting the net effect of midlatitude cyclones. Values in the top left of each panel represent the WCB (identified in the annual mean omega composite) integrated value (units of Tg d^{-1}).

To examine the net effect of cyclone WCBs on NH aerosol budgets, we integrate the enhancement in each term from Figure 11 for individual cyclones. Table 1 summarizes the annual totals (Tg yr^{-1}) for each aerosol component for each storm track. We find enhancements in the sulfate, organic carbon, and dust budget terms are a factor of 1.5-3 larger in North Pacific cyclones. Nevertheless, WCBs in both storm tracks display similar enhancement factors relative to background (Table 1). The annual cyclone-centered SSA budget is very similar between the

storm tracks. We find deposition by heavy precipitation in cyclone WCBs (Figure 2a) accounts for three-quarters of the overall deposition for sulfate, organic carbon, and dust while it accounts for only 20% for SSA deposition where settling (52%) plays a more significant role.

Table 1. Total annual enhancements in aerosol mass balance terms in the warm conveyor belts of northern hemisphere midlatitude cyclones in the North Atlantic and Pacific storm tracks (units of Tg yr^{-1}). The scavenging efficiency (Deposition / [Emission + Flux]) is also given for each component. Values in parentheses represent the enhancement factor relative to background.

	Sulfate	**Organic Carbon**	**Dust**	**Sea Salt**
		North Pacific		
Δ Emission	0.06 (-)	1.92 (-)	0.68 (-)	71.2 (2.12)
Δ Chemical Production	3.75 (2.40)	0 (-)	0 (-)	0 (-)
Δ Dry + Wet Deposition	6.96 (3.14)	3.49 (3.20)	8.28 (2.72)	73.97 (2.11)
Δ Horizontal Flux	7.01 (2.44)	6.5 (2.99)	26.7 (2.92)	26.57 (2.13)
Δ Burden	3.86 (1.37)	4.93 (1.57)	19.1 (1.43)	23.8 (1.79)
Scavenging Efficiency	0.99	0.42	0.31	0.76
		North Atlantic		
Δ Emission	0.05 (-)	0.3 (-)	1.18 (-)	61.5 (2.24)
Δ Chemical Production	1.81 (2.35)	0 (-)	0 (-)	0 (-)
Δ Dry + Wet Deposition	3.32 (3.14)	1.47 (3.12)	5.71 (3.07)	60.72 (2.23)
Δ Horizontal Flux	2.99 (2.40)	2.86 (3.26)	16.73 (2.97)	19.92 (2.13)
Δ Burden	1.53 (1.33)	1.69 (1.41)	12.2 (1.59)	20.7 (1.84)
Scavenging Efficiency	1.14	0.47	0.33	0.75

Because M2GMI does not treat secondary formation of organic carbon aerosol, all the WCB enhancement in its mass is due to transport from continental regions. Dust is the least efficiently scavenged aerosol species in cyclone WCBs due to its occurrence at higher altitudes (Figure 8-9). We find that the near-surface enhancements in SSA are due to the strong surface winds (Figure 2e) which cause large enhancements in emissions (Figure 10) and serve to advect SSA in the vicinity of the cyclone center.

7. Conclusions

Our analysis systematically examined aerosol distributions in midlatitude cyclones and linked processes in the WCB and broader cyclone environment to aerosol emissions and export to the

global atmosphere. The composites of 27,707 NH midlatitude cyclones over a 14-year period show a 25-50% increase in AOD observed by MODIS to the east of the cyclone center. These enhancements are co-located with heavy precipitation, extensive cloud cover, vertical motions, and high RH in the cyclone WCB. The M2GMI simulation shows a 30-50% increase in AOD in the same region. AOD and ΔAOD in cyclone WCBs maximize in spring due to a large contribution (> 70% of the total) from fine mode aerosols. Annually, export of fine aerosols accounts for 70% of the ΔAOD in MODIS and 63% in M2GMI. Overall, we find the M2GMI simulation captures the magnitude and seasonality of the MODIS observations (r = 0.97).

Composites of per species AOD from M2GMI reveal that cyclones enhance AOD by up to 40% for sulfate, 50% for organic carbon, 25% for dust, and 130% for SSA. The contribution of sulfate to the total ΔAOD is consistent throughout the year at 30-40%. The contribution of the other components shows large variability. The contribution of SSA ranges from 30% in fall-winter to < 10% in summer while the contribution of organic carbon ranges from < 10% in winter to > 50% in July and August. The contribution of dust maximizes at 20% in spring.

Examining vertical profiles of how each component contributes to the total Δ extinction reveals that SSA contributes almost half near the surface but only 14% overall. The contribution of sulfate is largest between 2-3 km (> 40%). Export of dust occurs at higher altitudes in cyclone WCBs: its contribution to Δ extinction maximizes in the free troposphere at about 4 km. We also find that aerosol growth due to RH accounts for half of the total ΔAOD in cyclone WCBs, ranging from 20% for SSA to 50-60% for sulfate and organic carbon.

We use our compositing approach to find that midlatitude cyclones account for 355 Tg yr^{-1} of SSA emissions annually. This constitutes 60% of the 30–80^{o} N emissions annually, ranging between 30% (summer) and 74% (winter). Our compositing approach also highlights the net effect of midlatitude cyclones on NH aerosol budgets. We find that largescale precipitation in cyclone WCBs efficiently removes > 90% of transported sulfate but only 30-40 % of organic carbon and dust. Therefore, net export of sulfate aerosol occurs due to chemical production in the cloudy WCB environment while organic carbon and dust export occurs as a result of large horizontal fluxes.

Aerosols remain a highly uncertain part of the climate future (Myhre et al., 2013) particularly due to changing anthropogenic emissions. As societies transition away from energy sources that emit greenhouse gases, it is likely that anthropogenic aerosol emission will also decrease (Larson & Portmann, 2019). Nevertheless, results from the Coupled Model Intercomparison Project Phase 6 project suggest increases in urban particulate matter even in scenarios with some climate mitigation actions (Turnock et al., 2020). In addition, transport pathways may change in the future as the spatiotemporal variability of midlatitude cyclones changes. While disagreement exists in projections of the NH storm tracks, one consistent projection is a seasonally non-uniform poleward shift (Simpson, Shaw, & Seager, 2014) coupled with an overall reduction in frequency (Chang, Guo, & Xia, 2012). Recent projections also suggest an increase in midlatitude cyclone precipitation under future climate scenarios (Catto et al., 2019) that could act to increase removal during transport. Taken together, these projections may suggest an overall reduction in aerosol export to the global atmosphere by cyclone WCBs with a simultaneous increase in aerosol abundances for the most polluted cyclones.

8. References

Alfaro, C., & Gomes, L. (2001). Modeling mineral aerosol production by wind erosion : Emission Particles enough. *Geophysical Research*, *106*(D16), 75–84.

Andreae, M. O., & Crutzen, P. J. (1997). Atmospheric aerosols: Biogeochemical sources and role in atmospheric chemistry. *Science*, *276*(5315), 1052–1058. https://doi.org/10.1126/science.276.5315.1052

Baker, A. R., Kelly, S. D., Biswas, K. F., Witt, M., & Jickells, T. D. (2003). Atmospheric deposition of nutrients to the Atlantic Ocean. *Geophysical Research Letters*, *30*(24), 2–5. https://doi.org/10.1029/2003GL018518

Bian, H., Chin, M., Hauglustaine, D. A., Schulz, M., Myhre, G., Bauer, S. E., … Tsyro, S. G. (2017). Investigation of global particulate nitrate from the AeroCom phase III experiment. *Atmospheric Chemistry and Physics*, *17*(21), 12911–12940. https://doi.org/10.5194/acp-17-12911-2017

Bian, H., Froyd, K., Murphy, D. M., Dibb, J., Darmenov, A., Chin, M., … Smirnov, A. (2019). Observationally constrained analysis of sea salt aerosol in the marine atmosphere. *Atmospheric Chemistry and Physics*, *19*(16), 10773–10785. https://doi.org/10.5194/acp-19-10773-2019

Booth, J. F., Naud, C. M., & Jeyaratnam, J. (2018). Extratropical Cyclone Precipitation Life Cycles: A Satellite-Based Analysis. *Geophysical Research Letters*, *45*(16), 8647–8654. https://doi.org/10.1029/2018GL078977

Brock, C. A., Hudson, P. K., Lovejoy, E. R., Sullivan, A., Nowak, J. B., Huey, L. G., … Wilson, J. C. (2004). Particle characterictics following cloud-modified transport from Asia to North America. *Journal of Geophysical Research D: Atmospheres*, *109*(23), 1–17. https://doi.org/10.1029/2003JD004198

Browning, K. A. (1997). The dry intrusion perspective of extra-tropical cyclone development. *Meteorological Applications*, *4*(4), S1350482797000613. https://doi.org/10.1017/S1350482797000613

Browning, K. A., & Roberts, N. M. (1994). Structure of a frontal cyclone. *Quarterly Journal of the Royal Meteorological Society*, *120*(520), 1535–1557. https://doi.org/10.1002/qj.49712052006

Catto, J. L., Ackerley, D., Booth, J. F., Champion, A. J., Colle, B. A., Pfahl, S., … Seiler, C. (2019). The Future of Midlatitude Cyclones. *Current Climate Change Reports*, *5*(4), 407–420. https://doi.org/10.1007/s40641-019-00149-4

Catto, J. L., Shaffrey, L. C., & Hodges, K. I. (2010). Can climate models capture the structure of extratropical

cyclones? *Journal of Climate*, *23*(7), 1621–1635. https://doi.org/10.1175/2009JCLI3318.1
Chang, E. K. M., Guo, Y., & Xia, X. (2012). CMIP5 multimodel ensemble projection of storm track change under global warming. *Journal of Geophysical Research Atmospheres*, *117*(23), 1–19. https://doi.org/10.1029/2012JD018578
Chang, E. K. M., & Song, S. (2006). The seasonal cycles in the distribution of precipitation around cyclones in the western north Pacific and Atlantic. *Journal of the Atmospheric Sciences*, 63(3), 815-839. https://doi.org/10.1175/JAS3661.1
Chin, M., Diehl, T., Tan, Q., Prospero, J. M., Kahn, R. A., Remer, L. A., … Torres, O. (2014). Multi-decadal aerosol variations from 1980 to 2009: A perspective from observations and a global model. *Atmospheric Chemistry and Physics*, *14*(7), 3657–3690. https://doi.org/10.5194/acp-14-3657-2014
Chin, Mian, Diehl, T., Dubovik, O., Eck, T. F., Holben, B. N., Sinyuk, A., & Streets, D. G. (2009). Light absorption by pollution, dust, and biomass burning aerosols: A global model study and evaluation with AERONET measurements. *Annales Geophysicae*, *27*(9), 3439–3464. https://doi.org/10.5194/angeo-27-3439-2009
Chin, Mian, Ginoux, P., Kinne, S., Torres, O., Holben, B. N., Duncan, B. N., … Nakajima, T. (2002). Tropospheric aerosol optical thickness from the GOCART model and comparisons with satellite and sun photometer measurements. *Journal of the Atmospheric Sciences*, *59*(3 PT 1), 461–483. https://doi.org/10.1175/1520-0469(2002)059<0461:taotft>2.0.co;2
Colarco, P., Da Silva, A., Chin, M., & Diehl, T. (2010). Online simulations of global aerosol distributions in the NASA GEOS-4 model and comparisons to satellite and ground-based aerosol optical depth. *Journal of Geophysical Research Atmospheres*, *115*(14). https://doi.org/10.1029/2009JD012820
Ding, A., Wang, T., Xue, L., Gao, J., Stohl, A., Lei, H., … Zhang, X. (2009). Transport of north China air pollution by midlatitude cyclones: Case study of aircraft measurements in summer 2007. *Journal of Geophysical Research Atmospheres*, *114*(8), 1–16. https://doi.org/10.1029/2008JD011023
Duncan, B. N., Strahan, S. E., Yoshida, Y., Steenrod, S. D., & Livesey, N. (2007). Model study of the cross-tropopause transport of biomass burning pollution. *Atmospheric Chemistry and Physics*, *7*(14), 3713–3736. https://doi.org/10.5194/acp-7-3713-2007
Dunlea, E. J., Decarlo, P. F., Aiken, A. C., Kimmel, J. R., Peltier, R. E., Weber, R. J., … Jimenez, J. L. (2009). Evolution of Asian aerosols during transpacific transport in INTEX-B. *Atmospheric Chemistry and Physics*, *9*(19), 7257–7287. https://doi.org/10.5194/acp-9-7257-2009
Eckhardt, S., Stohl, A., Wernli, H., James, P., Forster, C., & Spichtinger, N. (2004). A 15-year climatology of warm conveyor belts. *Journal of Climate*, *17*(1), 218–237. https://doi.org/10.1175/1520-0442(2004)017<0218:AYCOWC>2.0.CO;2
Eguchi, K., Uno, I., Yumimoto, K., Takemura, T., Shimizu, A., Sugimoto, N., & Liu, Z. (2009). Trans-pacific dust transport: Integrated analysis of NASA/CALIPSO and a global aerosol transport model. *Atmospheric Chemistry and Physics*, *9*(9), 3137–3145. https://doi.org/10.5194/acp-9-3137-2009
Fang, Y., Mauzerall, D. L., Liu, J., Fiore, A. M., & Horowitz, L. W. (2013). Impacts of 21st century climate change on global air pollution-related premature mortality. *Climatic Change*, *121*(2), 239–253. https://doi.org/10.1007/s10584-013-0847-8
Field, P. R., & Wood, R. (2007). Precipitation and cloud structure in midlatitude cyclones. *Journal of Climate*, *20*(2), 233–254. https://doi.org/10.1175/JCLI3998.1
Gelaro, R., McCarty, W., Suárez, M. J., Todling, R., Molod, A., Takacs, L., … Zhao, B. (2017). The Modern-Era Retrospective Analysis for Research and Applications, Version 2 (MERRA-2). *Journal of Climate*, *30*(14), 5419–5454. https://doi.org/10.1175/JCLI-D-16-0758.1
Ginoux, P., Chin, M., Tegen, I., Prospero, J. M., Holben, B., Dubovik, O., & Lin, S.-J. (2001). Sources and distributions of dust aerosols simulated with the GOCART model. *Journal of Geophysical Research: Atmospheres*, *106*(D17), 20255–20273. https://doi.org/10.1029/2000JD000053
Gong, S. L. (2003). A parameterization of sea-salt aerosol source function for sub- and super-micron particles. *Global Biogeochemical Cycles*, *17*(4), 1–7. https://doi.org/10.1029/2003gb002079
Graedel, T. E., & Weschler, C. J. (1981). Chemistry within aqueous atmospheric aerosols and raindrops. In *Reviews of Geophysics* (Vol. 19). https://doi.org/10.1029/RG019i004p00505
Grandey, B. S., Stier, P., Grainger, R. G., & Wagner, T. M. (2013). The contribution of the strength and structure of extratropical cyclones to observed cloud-aerosol relationships. *Atmospheric Chemistry and Physics*, *13*(21), 10689–10701. https://doi.org/10.5194/acp-13-10689-2013
Grandey, B. S., Stier, P., Wagner, T. M., Grainger, R. G., & Hodges, K. I. (2011). The effect of extratropical cyclones on satellite-retrieved aerosol properties over ocean. *Geophysical Research Letters*, *38*(13), 1–6. https://doi.org/10.1029/2011GL047703

Granier, C., Bessagnet, B., Bond, T., D'Angiola, A., van der Gon, H. D., Frost, G. J., … van Vuuren, D. P. (2011). Evolution of anthropogenic and biomass burning emissions of air pollutants at global and regional scales during the 1980-2010 period. *Climatic Change*, *109*(1), 163–190. https://doi.org/10.1007/s10584-011-0154-1

Grythe, H., Ström, J., Krejci, R., Quinn, P., & Stohl, A. (2014). A review of sea-spray aerosol source functions using a large global set of sea salt aerosol concentration measurements. *Atmospheric Chemistry and Physics*, *14*(3), 1277–1297. https://doi.org/10.5194/acp-14-1277-2014

Guibert, S., Matthias, V., Schulz, M., Bösenberg, J., Eixmann, R., Mattis, I., … Vaughan, G. (2005). The vertical distribution of aerosol over Europe - Synthesis of one year of EARLINET aerosol lidar measurements and aerosol transport modeling with LMDzT-INCA. *Atmospheric Environment*, *39*(16), 2933–2943. https://doi.org/10.1016/j.atmosenv.2004.12.046

Hannan, J. R., Fuelberg, H. E., Crawford, J. H., Sachse, G. W., & Blake, D. R. (2003). Role of wave cyclones in transporting boundary layer air to the free troposphere during the spring 2001 NASA/TRACE-P experiment. *Journal of Geophysical Research: Atmospheres*, *108*(20), 1–17. https://doi.org/10.1029/2002jd003105

He, H., Li, C., Loughner, C. P., Li, Z., Krotkov, N. A., Yang, K., … Dickerson, R. R. (2012). SO2 over central China: Measurements, numerical simulations and the tropospheric sulfur budget. *Journal of Geophysical Research Atmospheres*, *117*(3), 1–15. https://doi.org/10.1029/2011JD016473

Heald, C. L., Jacob, D. J., Park, R. J., Alexander, B., Fairlie, T. D., Yantosca, R. M., & Chu, D. A. (2006). Transpacific transport of Asian anthropogenic aerosols and its impact on surface air quality in the United States. *Journal of Geophysical Research Atmospheres*, *111*(14), 1–13. https://doi.org/10.1029/2005JD006847

Hess, M., Koepke, P., & Schult, I. (1998). Optical Properties of Aerosols and Clouds: The Software Package OPAC. *Bulletin of the American Meteorological Society*, *79*(5), 831–844. https://doi.org/10.1175/1520-0477(1998)079<0831:OPOAAC>2.0.CO;2

Hodzic, A., Kasibhatla, P. S., Jo, D. S., Cappa, C. D., Jimenez, J. L., Madronich, S., & Park, R. J. (2016). Rethinking the global secondary organic aerosol (SOA) budget: Stronger production, faster removal, shorter lifetime. *Atmospheric Chemistry and Physics*, *16*(12), 7917–7941. https://doi.org/10.5194/acp-16-7917-2016

Hoskins, B. J., & Hodges, K. I. (2002). New perspectives on the Northern Hemisphere winter storm tracks. *Journal of the Atmospheric Sciences*, *59*(6), 1041–1061. https://doi.org/10.1175/1520-0469(2002)059<1041:NPOTNH>2.0.CO;2

Huang, J., Minnis, P., Chen, B., Huang, Z., Liu, Z., Zhao, Q., … Ayers, J. K. (2008). Long-range transport and vertical structure of Asian dust from CALIPSO and surface measurements during PACDEX. *Journal of Geophysical Research Atmospheres*, *113*(23), 1–13. https://doi.org/10.1029/2008JD010620

Huebert, B. J., Bates, T., Russell, P. B., Shi, G., Kim, Y. J., Kawamura, K., … Nakajima, T. (2003). An overview of ACE-Asia: Strategies for quantifying the relationships between Asian aerosols and their climatic impacts. *Journal of Geophysical Research: Atmospheres*, *108*(23). https://doi.org/10.1029/2003jd003550

Isabel García, M., Rodríguez, S., & Alastuey, A. (2017). Impact of North America on the aerosol composition in the North Atlantic free troposphere. *Atmospheric Chemistry and Physics*, *17*(12), 7387–7404. https://doi.org/10.5194/acp-17-7387-2017

Jacobson, M. C., & Hansson, H. (2000). Review Ic Atmosph Eric Aerosols ' Science an D State of the. *Reviews of Geophysics*, (1998), 267–294. https://doi.org/10.1029/1998RG000045

Jaeglé, L., Quinn, P. K., Bates, T. S., Alexander, B., & Lin, J. T. (2011). Global distribution of sea salt aerosols: New constraints from in situ and remote sensing observations. *Atmospheric Chemistry and Physics*, *11*(7), 3137–3157. https://doi.org/10.5194/acp-11-3137-2011

Jaffe, D., McKendry, I., Anderson, T., & Price, H. (2003). Six "new" episodes of trans-Pacific transport of air pollutants. *Atmospheric Environment*, *37*(3), 391–404. https://doi.org/10.1016/S1352-2310(02)00862-2

Jickells, T. D., & Spokes, L. J. (2001). Atmospheric iron inputs to the oceans. In *The Biogeochemistry of Iron in Seawater* (pp. 85–121). Wiley.

Joos, H., Madonna, E., Witlox, K., Ferrachat, S., Wernli, H., & Lohmann, U. (2017). Effect of anthropogenic aerosol emissions on precipitation in warm conveyor belts in the western North Pacific in winter - A model study with ECHAM6-HAM. *Atmospheric Chemistry and Physics*, *17*(10), 6243–6255. https://doi.org/10.5194/acp-17-6243-2017

Kerminen, V. M., Lihavainen, H., Komppula, M., Viisanen, Y., & Kulmala, M. (2005). Direct observational evidence linking atmospheric aerosol formation and cloud droplet activation. *Geophysical Research Letters*, *32*(14), 1–4. https://doi.org/10.1029/2005GL023130

Kinne, S., Lohmann, U., Feichter, J., Schulz, M., Timmreck, C., Ghan, S., … Kaufman, Y. (2003). Monthly averages of aerosol properties: A global comparison among models, satellite data, and AERONET ground data. *Journal of Geophysical Research Atmospheres*, *108*(20). https://doi.org/10.1029/2001JD001253

Kunz, A., Pan, L. L., Konopka, P., Kinnison, D. E., & Tilmes, S. (2011). Chemical and dynamical discontinuity at the extratropical tropopause based on START08 and WACCM analyses. *Journal of Geophysical Research Atmospheres*, *116*(24), 1–15. https://doi.org/10.1029/2011JD016686

Larson, E. J. L., & Portmann, R. W. (2019). Anthropogenic aerosol drives uncertainty in future climate mitigation efforts. *Scientific Reports*, *9*(1), 1–8. https://doi.org/10.1038/s41598-019-52901-3

Levy, R. C., Mattoo, S., Munchak, L. A., Remer, L. A., Sayer, A. M., Patadia, F., & Hsu, N. C. (2013). The Collection 6 MODIS aerosol products over land and ocean. *Atmospheric Measurement Techniques*, *6*(11), 2989–3034. https://doi.org/10.5194/amt-6-2989-2013

Levy, Robert C., Remer, L. A., Tanré, D., Kaufman, Y. J., Ichoku, C., Holben, B. N., … Maring, H. (2003). Evaluation of the moderate-resolution imaging spectroradiometer (MODIS) retrievals of dust aerosol over the ocean during PRIDE. *Journal of Geophysical Research: Atmospheres*, *108*(19), 1–13. https://doi.org/10.1029/2002jd002460

Lewis, E. R., & Schwartz, S. E. (2004). *Sea Salt Aerosol Production: Mechanisms, Methods, Measurements* (E. R. Lewis & S. . Schwartz, eds.). Washington, DC: American Geophysical Union.

Liang, Q., Jaeglé, L., Jaffe, D. A., Weiss-Penzias, P., Heckman, A., & Snow, J. A. (2004). Long-range transport of Asian pollution to the northeast Pacific: Seasonal variations and transport pathways of carbon monoxide. *Journal of Geophysical Research D: Atmospheres*, *109*(23), 1–16. https://doi.org/10.1029/2003JD004402

Luan, Y., & Jaeglé, L. (2013). Composite study of aerosol export events from East Asia and North America. *Atmospheric Chemistry and Physics*, *13*(3), 1221–1242. https://doi.org/10.5194/acp-13-1221-2013

Madonna, E., Wernli, H., Joos, H., Martius, O. (2014). Warm conveyor belts in the ERA-Interim dataset (1979–2010). Part I: climatology and potential vorticity evolution. Journal of Climate, 27(1), 3-26. https://doi.org/10.1175/JCLI-D-12-00720.1

McCarty, W., Coy, L., Gelaro, R., Huang, A., Merkova, D., Smith, E.B., Sienkiewicz, M., Wargan, K. (2016). MERRA-2 input observations: Summary and assessment. *NASA/TM–2016–104606*, *46*, 64.

McCoy, D. T., Field, P. R., Schmidt, A., Grosvenor, D. P., Bender, F. A. M., Shipway, B. J., … Elsaesser, G. S. (2018). Aerosol midlatitude cyclone indirect effects in observations and high-resolution simulations. *Atmospheric Chemistry and Physics*, *18*(8), 5821–5846. https://doi.org/10.5194/acp-18-5821-2018

Molod, A., Takacs, L., Suarez, M., & Bacmeister, J. (2015). Development of the GEOS-5 atmospheric general circulation model: Evolution from MERRA to MERRA2. *Geoscientific Model Development*, *8*(5), 1339–1356. https://doi.org/10.5194/gmd-8-1339-2015

Myhre, G., Samset, B. H., Schulz, M., Balkanski, Y., Bauer, S., Berntsen, T. K., … Zhou, C. (2013). Radiative forcing of the direct aerosol effect from AeroCom Phase II simulations. *Atmospheric Chemistry and Physics*, *13*(4), 1853–1877. https://doi.org/10.5194/acp-13-1853-2013

Nam, J., Wang, Y., Luo, C., & Chu, D. A. (2010). Trans-Pacific transport of Asian dust and CO: Accumulation of biomass burning CO in the subtropics and dipole structure of transport. *Atmospheric Chemistry and Physics*, *10*(7), 3297–3308. https://doi.org/10.5194/acp-10-3297-2010

Naud, C. M., Booth, J. F., Jeyaratnam, J., Donner, L. J., Seman, C. J., Zhao, M., … Ming, Y. (2019). Extratropical cyclone clouds in the GFDL climate model: Diagnosing biases and the associated causes. *Journal of Climate*, *32*(20), 6685–6701. https://doi.org/10.1175/JCLI-D-19-0421.1

Naud, C. M., Posselt, D. J., & van den Heever, S. C. (2016). Aerosol optical depth distribution in extratropical cyclones over the Northern Hemisphere oceans. *Geophysical Research Letters*, *43*(19), 10,504-10,511. https://doi.org/10.1002/2016GL070953

Naud, C. M., Posselt, D. J., & van den Heever, S. C. (2017). Observed Covariations of Aerosol Optical Depth and Cloud Cover in Extratropical Cyclones. *Journal of Geophysical Research: Atmospheres*, *122*(19), 10,338-10,356. https://doi.org/10.1002/2017JD027240

Nielsen, J. E., Pawson, S., Molod, A., Auer, B., da Silva, A. M., Douglass, A. R., … Wargan, K. (2017). Chemical Mechanisms and Their Applications in the Goddard Earth Observing System (GEOS) Earth System Model. *Journal of Advances in Modeling Earth Systems*, *9*(8), 3019–3044. https://doi.org/10.1002/2017MS001011

Nowottnick, E., Colarco, P., Ferrare, R., Chen, G., Ismail, S., Anderson, B., & Browell, E. (2010). Online simulations of mineral dust aerosol distributions: Comparisons to namma observations and sensitivity to dust emission parameterization. *Journal of Geophysical Research Atmospheres*, *115*(3), 1–19. https://doi.org/10.1029/2009JD012692

Orbe, C., Oman, L. D., Strahan, S. E., Waugh, D. W., Pawson, S., Takacs, L. L., & Molod, A. M. (2017). Large-Scale Atmospheric Transport in GEOS Replay Simulations. *Journal of Advances in Modeling Earth Systems*, *9*(7), 2545–2560. https://doi.org/10.1002/2017MS001053

Park, R. J., Jacob, D. J., Palmer, P. I., Clarke, A. D., Weber, R. J., Zondlo, M. A., … Bond, T. C. (2005). Export

efficiency of black carbon aerosol in continental outflow: Global implications. *Journal of Geophysical Research D: Atmospheres*, *110*(11), 1–7. https://doi.org/10.1029/2004JD005432

Partanen, A. I., Landry, J. S., & Matthews, H. D. (2018). Climate and health implications of future aerosol emission scenarios. *Environmental Research Letters*, *13*(2). https://doi.org/10.1088/1748-9326/aaa511

Patoux, J., Yuan, X., & Li, C. (2009). Satellite-based midlatitude cyclone statistics over the Southern Ocean: 1. Scatterometer-derived pressure fields and storm tracking. *Journal of Geophysical Research*, *114*(D4). https://doi.org/10.1029/2008JD010873

Peltier, R. E., Hecobian, A. H., Weber, R. J., Stohl, A., Atlas, E. L., Riemer, D. D., … Karl, T. (2008). Investigating the sources and atmospheric processing of fine particles from Asia and the Northwestern United States measured during INTEX B. *Atmospheric Chemistry and Physics*, *8*(6), 1835–1853. https://doi.org/10.5194/acp-8-1835-2008

Platnick, S., King, M. D., Meyer, K. G., Wind, G., Amarasinghje, N., Marchant, B., … Riedi, J. (2015). *MODIS Cloud Optical Properties : User Guide for the Collection 6 Level-2 MOD06 / MYD06 Product and Associated Level-3 Datasets*. Retrieved from https://atmosphere-imager.gsfc.nasa.gov/sites/default/files/ModAtmo/C6MOD06OPUserGuide_0.pdf

Prather, K. A., Hatch, C. D., & Grassian, V. H. (2008). Analysis of atmospheric aerosols. *Annual Review of Analytical Chemistry*, *1*(1), 485–514. https://doi.org/10.1146/annurev.anchem.1.031207.113030

Randles, C. A., da Silva, A. M., Buchard, V., Colarco, P. R., Darmenov, A., Govindaraju, R., … Flynn, C. J. (2017). The MERRA-2 aerosol reanalysis, 1980 onward. Part I: System description and data assimilation evaluation. *Journal of Climate*, *30*(17), 6823–6850. https://doi.org/10.1175/JCLI-D-16-0609.1

Real, E., Pisso, I., Law, K. S., Legras, B., Bousserez, N., Schlager, H., … Attié, J. L. (2010). Toward a novel high-resolution modeling approach for the study of chemical evolution of pollutant plumes during long-range transport. *Journal of Geophysical Research Atmospheres*, *115*(12), 1–14. https://doi.org/10.1029/2009JD011707

Reichle, R. H., Liu, Q., Koster, R. D., Draper, C. S., Mahanama, S. P. P., & Partyka, G. S. (2017). Land Surface Precipitation in MERRA-2. *Journal of Climate*, *30*(5), 1643–1664. https://doi.org/10.1175/JCLI-D-16-0570.1

Remer, A, L., Kaufman, Y. J., Tanré, D., Mattoo, S., Chu, D. A., … and B N Holben. (2005). The MODIS Aerosol Algorithm, Products, and Validation. *Journal of the Atmospheric Sciences*, *62*(4), 947–973.

Remer, L. A., Kleidman, R. G., Levy, R. C., Kaufman, Y. J., Tanré, D., Mattoo, S., … Holben, B. N. (2008). Global aerosol climatology from the MODIS satellite sensors. *Journal of Geophysical Research Atmospheres*, *113*(14), 1–18. https://doi.org/10.1029/2007JD009661

Shindell, D. T., Lamarque, J. F., Schulz, M., Flanner, M., Jiao, C., Chin, M., … Lo, F. (2013). Radiative forcing in the ACCMIP historical and future climate simulations. *Atmospheric Chemistry and Physics*, *13*(6), 2939–2974. https://doi.org/10.5194/acp-13-2939-2013

Silva, R. A., West, J. J., Lamarque, J. F., Shindell, D. T., Collins, W. J., Faluvegi, G., … Zeng, G. (2017). Future global mortality from changes in air pollution attributable to climate change. *Nature Climate Change*, *7*(9), 647–651. https://doi.org/10.1038/nclimate3354

Simpson, I. R., Shaw, T. A., & Seager, R. (2014). A diagnosis of the seasonally and longitudinally varying midlatitude circulation response to global warming. *Journal of the Atmospheric Sciences*, *71*(7), 2489–2515. https://doi.org/10.1175/JAS-D-13-0325.1

Sinclair, V. A., Gray, S. L., & Belcher, S. E. (2008). Boundary-layer ventilation by baroclinic life cycles. *Quarterly Journal of the Royal Meteorological Society*, *134*(635), 1409–1424. https://doi.org/10.1002/qj.293

Smith, S. J., & Bond, T. C. (2014). Two hundred fifty years of aerosols and climate: The end of the age of aerosols. *Atmospheric Chemistry and Physics*, *14*(2), 537–549. https://doi.org/10.5194/acp-14-537-2014

Stohl, A. (2001). A 1-year Lagrangian "climatology" of airstreams in the Northern Hemisphere troposphere and lowermost stratosphere. *Journal of Geophysical Research Atmospheres*, *106*(D7), 7263–7279. https://doi.org/10.1029/2000JD900570

Strahan, S. E., Duncan, B. N., & Hoor, P. (2007). Observationally derived transport diagnostics for the lowermost stratosphere and their application to the GMI chemistry and transport model. *Atmospheric Chemistry and Physics*, *7*(9), 2435–2445. https://doi.org/10.5194/acp-7-2435-2007

Strode, S. A., Ziemke, J. R., Oman, L. D., Lamsal, L. N., Olsen, M. A., & Liu, J. (2019). Global changes in the diurnal cycle of surface ozone. *Atmospheric Environment*, *199*(August 2018), 323–333. https://doi.org/10.1016/j.atmosenv.2018.11.028

Turnock, S. T., Allen, R. J., Andrews, M., Bauer, S. E., Deushi, M., Emmons, L., … Zhang, J. (2020). Historical and future changes in air pollutants from CMIP6 models. *Atmospheric Chemistry and Physics*, *20*(23), 14547–14579. https://doi.org/10.5194/acp-20-14547-2020

Ulbrich, U., Leckebusch, G. C., & Pinto, J. G. (2009). *Extra-tropical cyclones in the present and future climate : a review*. 117–131. https://doi.org/10.1007/s00704-008-0083-8

Uno, I., Yumimoto, K., Shimizu, A., Hara, Y., Sugimoto, N., Wang, Z., … Winker, D. M. (2008). 3D structure of Asian dust transport revealed by CALIPSO lidar and a 4DVAR dust model. *Geophysical Research Letters*, *35*(6), 2–8. https://doi.org/10.1029/2007GL032329

Wang, Y., Zhang, R., & Saravanan, R. (2014). Asian pollution climatically modulates mid-latitude cyclones following hierarchical modelling and observational analysis. *Nature Communications*, *5*. https://doi.org/10.1038/ncomms4098

Wei, J., Li, Z., Peng, Y., & Sun, L. (2019). MODIS Collection 6.1 aerosol optical depth products over land and ocean: validation and comparison. *Atmospheric Environment*, *201*(October 2018), 428–440. https://doi.org/10.1016/j.atmosenv.2018.12.004

Wei, J., Peng, Y., Guo, J., & Sun, L. (2019). Performance of MODIS Collection 6.1 Level 3 aerosol products in spatial-temporal variations over land. *Atmospheric Environment*, *206*(September 2018), 30–44. https://doi.org/10.1016/j.atmosenv.2019.03.001

Weng, H., Lin, J., Martin, R., Millet, D. B., Jaeglé, L., Ridley, D., … Meng, J. (2020). Global high-resolution emissions of soil NOx, sea salt aerosols, and biogenic volatile organic compounds. *Scientific Data*, *7*(1), 1–15. https://doi.org/10.1038/s41597-020-0488-5

Wernli, H., & Schwierz, C. (2006). Surface cyclones in the ERA-40 dataset (1958-2001). Part I: Novel identification method and global climatology. *Journal of the Atmospheric Sciences*, *63*(10), 2486–2507. https://doi.org/10.1175/JAS3766.1

Westervelt, D. M., Horowitz, L. W., Naik, V., Golaz, J. C., & Mauzerall, D. L. (2015). Radiative forcing and climate response to projected 21st century aerosol decreases. *Atmospheric Chemistry and Physics*, *15*(22), 12681–12703. https://doi.org/10.5194/acp-15-12681-2015

Whitaker, J. S., Uccellini, L. W., & Brill, K. F. (1988). A Model-Based Diagnostic Study of the Rapid Development Phase of the Presidents's Day Cyclone. *Monthly Weather Review*, *116*(11), 2337–2365. https://doi.org/10.1175/1520-0493(1988)116<2337:AMBDSO>2.0.CO;2

Yang, Q., Easter, R. C., Campuzano-Jost, P., Jimenez, J. L., Fast, J. D., Ghan, S. J., … Wisthaler, A. (2015). Aerosol transport and wet scavenging in deep convective clouds: A case study and model evaluation using a multiple passive tracer analysis approach. *Journal of Geophysical Research: Atmospheres*, *120*(16), 8448–8468. https://doi.org/10.1002/2015JD023647

Yang, Y., Liao, H., & Lou, S. (2015). Decadal trend and interannual variation of outflow of aerosols from East Asia: Roles of variations in meteorological parameters and emissions. *Atmospheric Environment*, *100*, 141–153. https://doi.org/10.1016/j.atmosenv.2014.11.004

Yu, H., Remer, L. A., Chin, M., Bian, H., Kleidman, R. G., & Diehl, T. (2008). A satellite-based assessment of transpacific transport of pollution aerosol. *Journal of Geophysical Research*, *113*(D14), 1–15. https://doi.org/10.1029/2007jd009349

Zhang, R., Li, G., Fan, J., Wu, D. L., & Molina, M. J. (2007). Intensification of Pacific storm track linked to Asian pollution. *Proceedings of the National Academy of Sciences of the United States of America*, *104*(13), 5295–5299. https://doi.org/10.1073/pnas.0700618104